

On the statistical theory of self-gravitating collisionless dark matter flow: Scale and redshift variation of velocity and density distributions

Zhijie (Jay) Xu,¹★

¹Physical and Computational Sciences Directorate, Pacific Northwest National Laboratory; Richland, WA 99352, USA

Accepted XXX. Received YYY; in original form ZZZ

ABSTRACT

The statistics of velocity and density fields are crucial for cosmic structure formation and evolution. This paper extends our previous work on the two-point second-order statistics for the velocity field [Phys. Fluids 35, 077105 (2023)] to one-point probability distributions for both density and velocity fields. The scale and redshift variation of density and velocity distributions are studied by a halo-based non-projection approach. First, all particles are divided into halo and out-of-halo particles so that the redshift variation can be studied via generalized kurtosis of distributions for halo and out-of-halo particles, respectively. Second, without projecting particle fields onto a structured grid, the scale variation is analyzed by identifying all particle pairs on different scales r . We demonstrate that: i) Delaunay tessellation can be used to reconstruct the density field. The density correlation, spectrum, and dispersion functions were obtained, modeled, and compared with the N-body simulation; ii) the velocity distributions are symmetric on both small and large scales and are non-symmetric with a negative skewness on intermediate scales due to the inverse energy cascade on small scales with a constant rate ε_u ; iii) On small scales, the even order moments of pairwise velocity Δu_L follow a two-thirds law $\propto (-\varepsilon_u r)^{2/3}$, while the odd order moments follow a linear scaling $\langle (\Delta u_L)^{2n+1} \rangle = (2n+1) \langle (\Delta u_L)^{2n} \rangle \langle \Delta u_L \rangle \propto r$; iv) The scale variation of the velocity distributions was studied for longitudinal velocities u_L or u'_L , pairwise velocity (velocity difference) $\Delta u_L = u'_L - u_L$ and velocity sum $\Sigma u_L = u'_L + u_L$. Fully developed velocity fields are never Gaussian on any scale, despite that they can initially be Gaussian; v) On small scales, u_L and Σu_L can be modeled by a X distribution to maximize the entropy of the system. The distribution of Δu_L can be different; vi) On large scales, Δu_L and Σu_L can be modeled by a logistic or a X distribution, while u_L has a different distribution; vii) the redshift variation of the velocity distributions follows the evolution of the X distribution involving a shape parameter $\alpha(z)$ decreasing with time.

CONTENTS

- 1 Introduction
- 2 N-body simulations and numerical data
- 3 Statistical measures of velocity field
 - 3.1 Pair conservation equation and algorithm validation
 - 3.2 Generalized kurtosis, moments, and structure functions
 - 3.3 Generalized kurtosis from N-body simulation
 - 3.4 First order moment of velocity
 - 3.5 Second order moment of velocity
 - 3.6 Even order moments and two-thirds law
 - 3.7 Odd order moments and stable clustering hypothesis
- 4 Probability distributions of velocity field
 - 4.1 Velocity distributions on small scales
 - 4.2 Distribution of pairwise velocity on small scales
 - 4.3 Velocity distributions on intermediate scales
 - 4.4 Velocity distributions on large scales
 - 4.5 Redshift evolution of velocity distributions
- 5 Probability distributions of density field
 - 5.1 One-point probability distributions
 - 5.2 Two-point second-order statistical measures
 - 5.3 Models for second-order statistical measures
- 6 Conclusions

1 INTRODUCTION

Many astronomical observations support the existence of dark matter. In standard Λ CDM cosmology, the amount of dark matter is about five times that of baryonic matter [1, 2, 3]. Therefore, the flow of dark matter has a wide presence in our universe. In contrast to the conventional collisional hydrodynamics, self-gravitating collisionless fluid dynamics (SG-CFD) concerns the dynamics and statistics of the velocity and density fields of collisionless dark matter, which provides valuable information for the large-scale structure formation and constraining cosmological parameters [4]. Our previous work mainly focuses on the two-point second-order statistical correlations and kinematic relations for the velocity field of dark matter flow [5]. Later, high-order two-point statistics and relevant kinematic and dynamic relations were developed in [6]. We demonstrate a scale-dependent nature of dark matter flow, e.g., a constant divergence flow on small scales and an irrotational flow on large scales (Fig. 1). In this paper, the statistical analysis is extended to the one-point probability distributions of velocity and density fields and their scale and redshift variation, e.g., distributions at different scales and redshifts.

The cosmic velocity and density fields contain rich information for structure formation and evolution. Velocities of galaxies are a robust probe for the search of dark matter on large scales [7], where statistical analysis can be performed based on galaxy number weighted statistics [8, 9]. Statistical analysis of velocity fields was also applied to describe the evolution of a system of self-gravitating collisionless particles using BBGKY equations [10]. Pairwise velocity has been

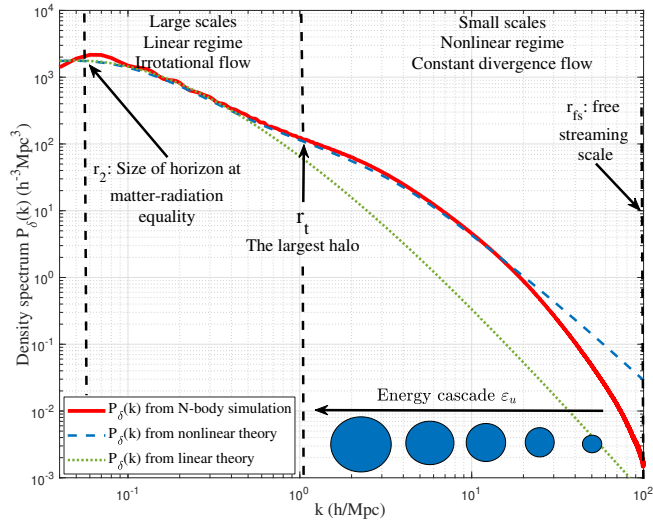


Figure 1. The variation of density power spectrum $P_\delta(k)$ with comoving wavenumber k at $z=0$ from a N-body simulation. Linear and non-linear theory predictions are also presented for comparison. The pivot wavenumber k_{\max} (or pivot scale $r_2=21.3 \text{ Mpc}/h$ [5]) denotes the size of the horizon at the matter-radiation equality. The scale $r_t \approx 1 \text{ Mpc}/h$ is roughly the size of the largest halo. The scale r_{fs} represents the free streaming scales for the smallest haloes that depend on dark matter particle properties. Dark matter flow is irrotational on large scales $r > r_t$ (linear regime) and constant divergence on small scales $r_{fs} < r < r_t$ (nonlinear regime), along with a smooth transition around scale r_t [5]. On small scales $r < r_t$ (nonlinear regime), there exists a halo-mediated energy cascade with a constant rate of ε_u , which can be used to derive halo mass functions, density profiles [25], and dark matter particle properties [26]. This paper focuses on the one-point probability distributions of dark matter velocity and density fields and their variation with redshifts and scales (e.g., distributions on small, intermediate, and large scales).

introduced to probe the cosmological density parameter [11, 12], and the two-point correlation function has been introduced to quantify the cosmic velocity field from the real dataset [13, 14]. The density statistics, including the matter density distributions, are important for gravitational lensing and nonlinear clustering. The study of matter density has a long history dating back to the 1930s when Hubble found that the matter distribution is non-Gaussian and can be approximated by a log-normal distribution [15]. Interests and efforts are still ongoing both theoretically and numerically [16, 17].

In addition, the velocity statistics have profound implications for direct/indirect detection. For predicted DM-nucleon scattering in direct detection [18, 19], the detection rate of the scattering is proportional to the inverse moment of distribution (or order of -1). That rate is very sensitive to the high-velocity tail of the velocity distribution. For indirect search [20, 21], the annihilation cross section depends directly on the distribution of relative velocity. The velocity distribution of dark matter particles is expected to be different from Maxwell-Boltzmann. This can be confirmed by N-body simulations [22, 23] and by our previous work on the maximum entropy distributions in dark matter flow [24].

Cosmic velocity and density fields exhibit a different nature on different scales. To illustrate this, Figure 1 presents the density power spectrum $P_\delta(k)$ as a function of the comoving wavenumber k from a N-body simulation (solid red line) [27]. The corresponding predictions from linear theory (dotted green line) and nonlinear theory (dashed blue line) are also presented [28]. There are three distinct scales in this figure. The comoving length scale r_2 or the pivot

wavenumber k_{\max} ($k_{\max} r_2 = \sqrt{2}$ [5]) is related to the horizon size at the matter-radiation equality, where $k_{\max} \propto \Omega_m h^2$ is proportional to the content of matter Ω_m . The length scale $r_t \approx 1 \text{ Mpc}/h$ is roughly the size of the largest halo at $z = 0$ [5]. The linear theory is valid only on large scales $r > r_t$ and underestimates the power spectrum on small scales. The free streaming scale r_{fs} represents the scale of the smallest structure due to the thermal velocity of dark matter particles. This scale depends heavily on the properties and nature of dark matter. A detailed analysis of the free streaming scale is presented in a separate work [26]. On small scales ($r_{fs} < r < r_t$) in the highly nonlinear regime, haloes have a vanishing (proper) radial flow. The peculiar velocity \mathbf{u} satisfies a (spatially) constant divergence or $\nabla \cdot \mathbf{u} = -3Ha$, where H is the Hubble parameter and a is the scale factor [29]. On large scales ($r > r_t$) in the linear regime, the flow becomes irrotational or $\nabla \times \mathbf{u} = 0$. The different nature of flow on various scales is a unique feature of the self-gravitating collisionless dark matter flow (SG-CFD) that is different from conventional hydrodynamic turbulence [5]. In this paper, we focus on the velocity and density distributions on small ($r < r_t$), intermediate ($r \approx r_t$), and large scales ($r > r_t$), respectively.

Directly measuring velocity and density fields from real samples is still very challenging. However, tremendous information can be obtained from N-body simulations, an invaluable tool for studying the dynamics of collisionless dark matter flow in both linear and nonlinear regimes [30, 31, 32, 33]. However, it is not trivial to extract and characterize the statistics of velocity and density fields from N-body simulations. There is a fundamental problem as velocity and density are only sampled at discrete locations of the particle position in N-body simulations. That sampling has poor quality at locations with low particle density [34]. The standard approach computes the power spectrum of the velocity and density fields (and gradients) in Fourier space [35, 36, 37], where cloud-in-cell (CIC) [38] or triangular-shaped-cloud (TSC) schemes are used to project the density and velocity fields onto regular structured grids. This will unavoidably introduce sampling errors in the density and velocity fields [39, 40].

Since real-space and Fourier-space data contain the same information, directly working with real-space data can avoid information loss due to field projection and the conversion between Fourier-space and real-space. In this paper, a halo-based non-projection approach is applied for statistical analysis of density and velocity fields:

- (i) Instead of projecting particle fields onto the structured grid, analysis is performed in real space by computing the statistics (second or high orders) for all particle pairs with a given separation r (shown in Fig. 2). The scale-dependent nature of these statistics can be studied efficiently as a function of scale r . This will maximally preserve and utilize the information contained in N-body simulations;
- (ii) Based on the halo description of the N-body system, dark matter particles continuously form halo structures. In this paper, all haloes in the N-body system are identified, and all particles are divided into halo and out-of-halo particles. We focus on relevant statistics for all halo particles and out-of-halo particles, respectively. Since the critical scale r_t stands for the size of the largest haloes, the statistics for all halo particles represent the average statistics on small scales $r < r_t$. While the statistics for out-of-halo particles represent the average statistics on large scales $r > r_t$.

From this practice, a huge amount of knowledge can be learned for self-gravitating collisionless fluid dynamics (SG-CFD) when compared with the isotropic, homogeneous, and incompressible turbulence [41, 42, 43, 44]. An example is the pairwise velocity ($\Delta u_L = u'_L - u_L$, see Fig. 2). For incompressible isotropic turbulence, there exists an inertial range of scales with a constant energy

flux ε_u , followed by a dissipation range dominated by the viscous force due to the viscosity of the liquid. A simple but universal form has been established for the m th order longitudinal velocity structure function (or the m th moment of pairwise velocity in cosmology terms) in the inertial range [45]. For incompressible isotropic turbulence, the m th moment of pairwise velocity reads

$$\begin{aligned} S_m^{LP}(r) &= \langle \Delta u_L^m \rangle = \langle (u'_L - u_L)^m \rangle = \beta_m (\varepsilon_u)^{m/3} r^{m/3}, \\ S_2^{LP}(r) &= \beta_2 \varepsilon_u r^{2/3} \quad \text{and} \quad S_3^{LP}(r) = -4/5 \varepsilon_u r, \end{aligned} \quad (1)$$

where u'_L and u_L are longitudinal velocities in Fig. 2, β_m is a universal constant, and ε_u is the rate of energy cascade (energy flux across different scales). Specifically, for $m = 2$, constant $\beta_2 \approx 2$. This is known as the two-thirds law, where the second-order structure function (or pairwise velocity dispersion in cosmology) satisfies $S_2^{LP}(r) \propto r^{2/3}$. A different scaling $S_2^{LP}(r) \propto r^2$ works in the dissipation range where the effects of viscosity are dominant. For $m = 3$, $\beta_3 = -4/5$. The third-order structure function satisfies $S_3^{LP}(r) = -4/5 \varepsilon_u r$. This is known as the four-fifths law that can be precisely derived from the Navier-Stokes equation [43]. Similarly, a different scaling $S_3^{LP}(r) \propto r^3$ works in the dissipation range.

However, the dark matter flow exhibits different behaviors due to its collisionless nature and long-range gravitational interactions, which leads to different scaling laws and behaviors on different scales. Using the halo-based non-projection approach, we can

- (i) study the scale and redshift variation of velocity and density distributions via the variation of generalized kurtosis (Eq. (7));
- (ii) demonstrate that velocity fields are non-Gaussian on all scales despite that they can be initially Gaussian (Fig. 5);
- (iii) analytically model velocity distributions on small and large scales, respectively;
- (iv) identify a universal two-thirds law for even order structure functions in Fig. 11 and a liner scaling law for odd order structure functions in Fig. 12 (generalized stable clustering hypothesis GSCH);
- (v) obtain the redshift evolution of one-point density and log-density distributions for halo and out-of-halo particles and analytical models for two-point density correlations;

The paper is organized as follows: Section 2 introduces the N-body simulation, followed by the statistical measures of the velocity field in Section 3. The redshift and scale dependence of the velocity distributions are presented and modeled in Section 4, as well as a comparison with N-body simulations. The statistical measures and distributions for the density field are presented and modeled in Section 5.

2 N-BODY SIMULATIONS AND NUMERICAL DATA

The numerical data was publicly available and generated from the N-body simulations carried out by the Virgo consortium. A comprehensive description of the data can be found in [27, 28]. As a first step, the current study was carried out using simulation runs with $\Omega=1$ and the standard CDM power spectrum (SCDM) that started from $z = 50$ to focus on the matter-dominant self-gravitating flow of collisionless dark matter. Similar analysis can be extended to other simulations with different cosmological assumptions and parameters in the future. The same set of data has been widely used in studies from clustering statistics [28] to formation of cluster haloes in a large-scale environment [46], and in the testing of models for halo abundances and mass functions [47]. Some key numerical parameters of the N-body simulation are listed in Table 1.

Table 1. Numerical parameters of SCDM N-body simulation

Run	Ω_0	Λ	h	Γ	σ_8	L (Mpc/h)	N	m_p M_\odot/h	l_{soft} (Kpc/h)
SCDMI	1.0	0.0	0.5	0.5	0.51	239.5	256^3	2.27×10^{11}	36

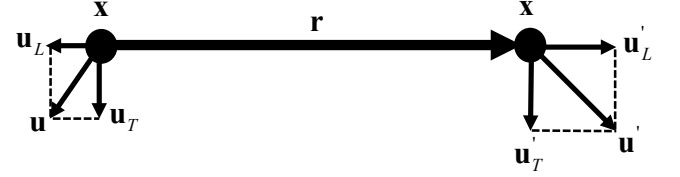


Figure 2. Two particles form a pair with a separation of scale r . The longitudinal (u_L) and transverse (u_T) velocities on scale r can be calculated from the projection of particle velocity (\mathbf{u}) on to vector of separation \mathbf{r} (Eq. (2)). In this paper, we focus on the scale dependence (r -dependence) of various statistical measures and distributions of the velocity field.

In this paper, a new approach is applied to directly compute the real-space statistics by pairwise averaging over all particle pairs on a given scale r . This approach can maximally employ the information contained in N-body simulation and generate complete statistics on all scales without involving any projection kernels (e.g., CIC). However, it is also computationally intensive to identify all pairs of particles on all scales. The selected N-body simulation has a relatively low resolution compared with other recent cosmological simulations. This enables a computationally affordable direct extraction of real-space two-point statistics. With increasing computing power, the same approach can be similarly extended to other simulations with higher resolution and higher-order statistics.

3 STATISTICAL MEASURES OF VELOCITY FIELD

To understand how velocity distributions vary with scale r and redshift z , we are interested in three types of velocities on different scales, i.e. the longitudinal velocity u_L or u'_L , the velocity difference (or pairwise velocity) $\Delta u_L = u'_L - u_L$, and the velocity sum $\Sigma u_L = u_L + u'_L$. In Fig. 2, for a pair of particles with velocities \mathbf{u} and \mathbf{u}' , and a vector of separation $\mathbf{r} = \mathbf{x}' - \mathbf{x}$, the longitudinal and transverse velocities are

$$\begin{aligned} u_L &= \mathbf{u} \cdot \hat{\mathbf{r}} \quad \text{and} \quad \mathbf{u}_T = -(\mathbf{u} \times \hat{\mathbf{r}} \times \hat{\mathbf{r}}) = \mathbf{u} - (\mathbf{u} \cdot \hat{\mathbf{r}}) \hat{\mathbf{r}}, \\ u'_L &= \mathbf{u}' \cdot \hat{\mathbf{r}} \quad \text{and} \quad \mathbf{u}'_T = -(\mathbf{u}' \times \hat{\mathbf{r}} \times \hat{\mathbf{r}}) = \mathbf{u}' - (\mathbf{u}' \cdot \hat{\mathbf{r}}) \hat{\mathbf{r}}, \end{aligned} \quad (2)$$

where $\hat{\mathbf{r}} = \mathbf{r}/r$ is the normalized unit vector.

For any given scale r , all particle pairs with a separation between r and $r+dr$ ($dr = 0.001 Mpc/h$ in this work) are identified, and the positions and velocities of the particles are recorded. Statistical quantities can be calculated by averaging that quantity on all pairs of particles on the same scale r . By this approach, the information contained in N-body simulations is maximally preserved without projecting particle velocity onto a structured grid.

In addition to three types of longitudinal velocities that are scale-dependent (u_L or u'_L , Δu_L , and Σu_L), we are also interested in the distributions of four velocities based on the halo description. These velocities are the velocity of all particles in the entire system (\mathbf{u}_p), the velocity of all halo particles (\mathbf{u}_{hp}), the velocity of all out-of-halo particles (\mathbf{u}_{op}), and the velocity of all haloes identified in the

system (\mathbf{u}_h , the mean velocity of all particles in the same halo). The distributions of these velocities are dependent on the redshift z . In addition, the velocity of halo particles represents the velocity on small scales $r < r_t$, while the velocity of out-of-halo particles and haloes represents the velocity on large scales $r > r_t$ (Fig. 1). The redshift and scale variation of these distributions will significantly improve our understanding of dark matter flow.

3.1 Pair conservation equation and algorithm validation

To validate the algorithm that identifies all particle pairs with a given separation r , we compare the mean pairwise velocity $\langle \Delta u_L \rangle$ to the pair conservation equation that relates the mean pairwise velocity with the density correlation [48],

$$\frac{\langle \Delta u_L \rangle}{Har} = -\frac{(1 + \bar{\xi}(r, a))}{3(1 + \xi(r, a))} \frac{\partial \ln(1 + \bar{\xi}(r, a))}{\partial \ln a}, \quad (3)$$

where $\bar{\xi}(r, a) = 3r^{-3} \int_0^r \xi(y, a) y^2 dy$ is the volume averaged density correlation (Eq. (87)). On large scales in the linear regime, $\bar{\xi} \ll 1$ and $\partial \ln \bar{\xi} / \partial \ln a = 2$, Eq. (3) reduces to

$$\frac{\langle \Delta u_L \rangle}{Har} = -\frac{2\bar{\xi}(r, a)(1 + \bar{\xi}(r, a))}{3(1 + \xi(r, a))} \approx -\frac{2}{3}\bar{\xi}(r, a). \quad (4)$$

On small scales in the nonlinear regime with $\bar{\xi} \gg 1$ and assuming the scaling with scale factor as $\xi(r, a) \propto a^\alpha$ (Fig. 30) and $\partial \ln \bar{\xi} / \partial \ln a = \alpha$, the pair conservation Eq. (3) reduces to

$$\frac{\langle \Delta u_L \rangle}{Har} = -\frac{\alpha(1 + \bar{\xi}(r, a))}{3(1 + \xi(r, a))}. \quad (5)$$

On small scales, if stable clustering hypothesis ($\langle \Delta u_L \rangle = -Har$) (demonstrated in [49]) is assumed and considering a self-similar gravitational clustering $\xi(r, a) \propto a^\alpha r^\gamma$, we have

$$\frac{\langle \Delta u_L \rangle}{Har} = -1 \quad \text{and} \quad \alpha = \gamma + 3, \quad (6)$$

where the exponents α and γ are related to each other.

Figure 3 plots the variation of the mean pairwise velocity $\langle \Delta u_L \rangle$ with scale r (normalized by the Hubble constant) at $z=0$. The results are compared with the prediction of the pair conservation equation for both linear (black dashed line from Eq. (4)) and nonlinear regime (red dashed line from Eq. (5) with $\alpha = 5/2$ from Fig. 30) using the density correlation $\xi(r, a)$ obtained from the N-body simulation (Fig. 29). The blue line is the normalized pairwise velocity computed directly from the N-body simulation by identifying all particle pairs and associated velocities. A good match with the pair conservation equation validates our numerical implementation to identify all pairs of particles on any fixed scale r .

3.2 Generalized kurtosis, moments, and structure functions

The velocity distributions can be best characterized by dimensionless generalized kurtosis. An example is the generalized kurtosis for the distribution of velocity difference Δu_L (or pairwise velocity). On any scale of r , the generalized kurtosis reads

$$K_n(\Delta u_L, r) = \frac{\langle (\Delta u_L - \langle \Delta u_L \rangle)^n \rangle}{\langle (\Delta u_L - \langle \Delta u_L \rangle)^2 \rangle^{n/2}} = \frac{S_n^{cP}(\Delta u_L, r)}{S_2^{cP}(\Delta u_L, r)^{n/2}}, \quad (7)$$

where the central moment of order n for Δu_L reads

$$S_n^{cP}(\Delta u_L, r) = \langle (\Delta u_L - \langle \Delta u_L \rangle)^n \rangle. \quad (8)$$

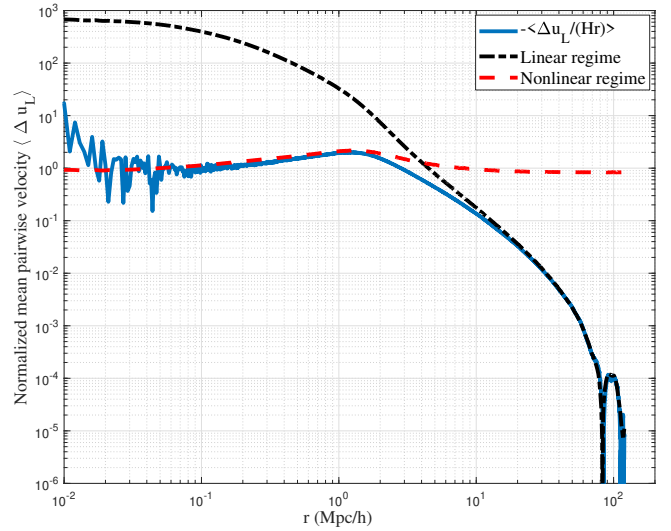


Figure 3. The variation of mean pairwise velocity $\langle \Delta u_L \rangle$ with scale r at $z=0$ (normalized by Hubble constant H) from N-body simulation (blue solid). Results are compared with predictions of pair conservation equation for both linear (black dashed dashed from Eq. (4)) and nonlinear regime (red dash from Eq. (5)). Predictions are made with the density correlation $\xi(r)$ obtained from the same N-body simulation.

On the same scale r , the n th order longitudinal structure function of Δu_L is defined as the n th order moment

$$S_n^{lP}(r) = \langle (\Delta u_L)^n \rangle = \langle (u'_L - u_L)^n \rangle. \quad (9)$$

Specifically, the first order structure function is just the mean pairwise velocity $\langle \Delta u_L \rangle$.

Remarks: For incompressible hydrodynamics, the mean velocities $\langle u_L \rangle = \langle \Delta u_L \rangle = \langle \Sigma u_L \rangle = 0$ on all scales of r such that $S_n^{cP}(\Delta u_L, r) = S_n^{lP}(r)$. The central moment of Δu_L equals the structure function defined in Eq. (9). However, for self-gravitating collisionless dark matter flow (SG-CFD), two particles tend to approach each other under gravity that leads to a non-zero mean longitudinal velocity $\langle u_L \rangle = -\langle \Delta u_L \rangle / 2 > 0$. Therefore, the central moment $S_n^{cP}(\Delta u_L, r) \neq S_n^{lP}(r)$ for SG-CFD. The distributions of longitudinal velocity u_L and pairwise velocity Δu_L are symmetric on small and large scales ($\langle \Delta u_L \rangle = 0$ on scales $r \ll r_t$ and $r \gg r_t$). Distributions of Δu_L and u_L can be asymmetric with non-vanishing odd-order moments on intermediate scales $r \approx r_t$ (Fig. 16). Due to symmetry, the mean $\langle \Sigma u_L \rangle = 0$. The distribution of Σu_L is always symmetric on any scale r with vanishing odd-order moments.

3.3 Generalized kurtosis from N-body simulation

Figure 4 presents the time variation of generalized kurtosis for velocity \mathbf{u}_p (for all particles), \mathbf{u}_{hp} (for halo particles) and \mathbf{u}_{op} (for out-of-halo particles). Different orders of kurtosis for the Gaussian distribution are plotted as dashed green lines for comparison. All velocities are initially Gaussian. The distribution of the halo particle velocity \mathbf{u}_{hp} deviates from the Gaussian much faster than the distribution of the out-of-halo particle velocity \mathbf{u}_{op} due to much stronger gravitational interactions in the haloes than the gravity between the haloes. All velocities become non-Gaussian with time to maximize the entropy of the system [24].

Figure 5 plots the even-order generalized kurtosis (4^{th} order –

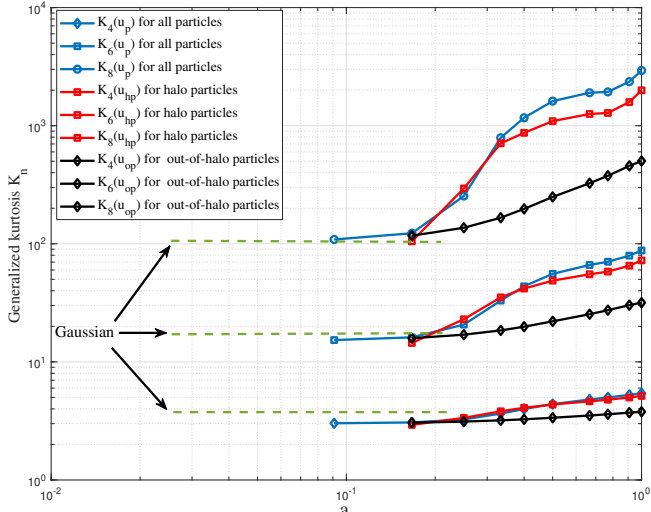


Figure 4. The variation of generalized kurtosis (even order) with scale factor a for the velocity of all particles (u_p : blue), all halo particles (u_{hp} : red), and all out-of-halo particles (u_{op} : black). Gaussian distribution is presented as green dashed lines. Since the Gaussian distribution is not the maximum entropy distribution of dark matter flow [24], all velocities are initially Gaussian and quickly become non-Gaussian with increasing kurtosis to maximize entropy. The evolution of the distribution of the out-of-halo particle velocity is much slower than that of the halo particles due to weak gravity on large scales.

bottom, 6^{th} order – middle, and 8^{th} order – top) of three velocities (u_L , Δu_L and Σu_L) at $z=0$. The 4^{th} , 6^{th} , and 8^{th} order kurtosis of the Gaussian distribution (magenta) is also plotted in the same figure with $K_4 = 3$, $K_6 = 15$, and $K_8 = 105$. Clearly, distributions of three velocities are non-Gaussian on all scales due to the long-range nature of gravity. This is important as it poses serious challenges to any theory that assumes the Gaussianity of velocity fields. The velocity field of fully developed self-gravitating collisionless dark matter flow (SG-CFD) is non-Gaussian on any scale, despite the fact that they can initially be Gaussian. In contrast, for incompressible hydrodynamics with short-range interactions, the distribution of velocity u_L is nearly Gaussian on large scales. Distributions of Δu_L are also Gaussian on large scales and only become non-Gaussian in the dissipation range because of the viscous force (Table 2).

In Fig. 5, the distribution of Σu_L approaches the distribution of u_L on small scales with a limiting correlation (between u_L and u'_L), where $\rho_L = \langle u'_L u_L \rangle / \langle u_L^2 \rangle = 0.5$ between two velocities [see ref. 5, Fig. 17]. As $r \rightarrow 0$, and the sum velocity $\lim_{r \rightarrow 0} \Sigma u_L = \lim_{r \rightarrow 0} (u'_L + u_L)$ will become the total velocity \mathbf{u} at location x . Longitudinal velocities u_L and u'_L along many different directions will simply collapse into velocity \mathbf{u} , and this also requires $\rho_L = 0.5$, i.e.

$$\begin{aligned} \lim_{r \rightarrow 0} \left\langle \left(u'_L + u_L \right)^2 \right\rangle &= \lim_{r \rightarrow 0} \left(\langle u_L'^2 \rangle + \langle u_L^2 \rangle + 2 \langle u'_L u_L \rangle \right) \\ &= \lim_{r \rightarrow 0} |\mathbf{u}(x)|^2 = 3 \lim_{r \rightarrow 0} \langle u_L^2 \rangle. \end{aligned} \quad (10)$$

On large scales, the distribution of Σu_L approaches the distribution of Δu_L with correlation $\rho_L = 0$ between u_L and u'_L . This is also expected, as the sum and difference of two independent random variables with symmetric distributions should follow the same distribution. Finally, on both small and large scales, generalized kurtosis approaches a constant so that there exist unique (limiting) probability distributions that are independent of scale r when $r \rightarrow 0$ or $r \rightarrow \infty$.

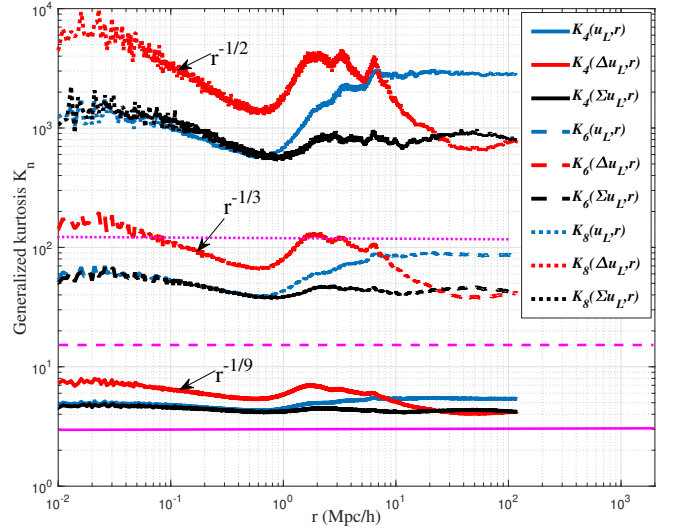


Figure 5. The even order generalized kurtosis (4^{th} , 6^{th} , and 8^{th} order) of three velocities varying with scale r at $z=0$. The generalized kurtosis of Gaussian distribution is plotted in magenta for comparison. All velocity distributions are non-Gaussian on all scales due to the long-range gravitational interaction, despite the fact that they can be initially Gaussian. The distribution of Σu_L approaches that of u_L on small scales, while the distribution of Σu_L approaches that of Δu_L on large scales. There exist limiting probability distributions for all velocities on both small and large scales.

On an intermediate scale of around $r_t = 1 \text{ Mpc/h}$, all three velocity distributions exhibit the greatest value of generalized kurtosis. The velocity distributions on small, intermediate, and large scales from simulation and theory are presented in Section 4.

Figure 6 plots the scale variation of odd-order generalized kurtosis (K_3 and K_5) with scale r at $z=0$ for pairwise velocity Δu_L . Odd-order kurtosis vanishes on both small and large scales, where the distribution of Δu_L is symmetric. The skewness $K_3(\Delta u_L, r) < 0$ on the intermediate scale $r = r_t$ (the distribution of Δu_L skews toward the positive side; see Fig. 16). Negative skewness is an important signature of the inverse cascade of kinetic energy on small scales $r < r_t$ (Fig. 1) that might lead to the negative "effective" viscosity on large scales $r > r_t$ [6]. For hydrodynamic turbulence, the negative skewness takes place in the dissipation range, where energy is cascaded from large to small scales and destroyed by viscosity.

3.4 First order moment of velocity

While generalized kurtosis can be used to characterize the distributions of different velocities, the moments of velocity distributions can be studied in detail to provide more insight. Due to symmetry, the first-order moment of the velocity sum $\langle \Sigma u_L \rangle = 0$ vanishes on all scales. This section focuses on the first-order moment of pairwise velocity, e.g., the first-order structure function $S_1^{1P}(r) = \langle \Delta u_L \rangle$ in Eq. (9). On small scales, an exact expression can be identified from the stable clustering hypothesis,

$$\langle \Delta u_L \rangle = -Har \quad \text{and} \quad \langle u_L \rangle = Har/2. \quad (11)$$

For nonlinear regime below the critical scale $r_t = 1.3a^{1/2} \text{ Mpc/h}$ where the longitudinal velocity correlation equals the transverse velocity correlation [see ref. 5, Figs. 3, 4, and 5], a better relation to fit

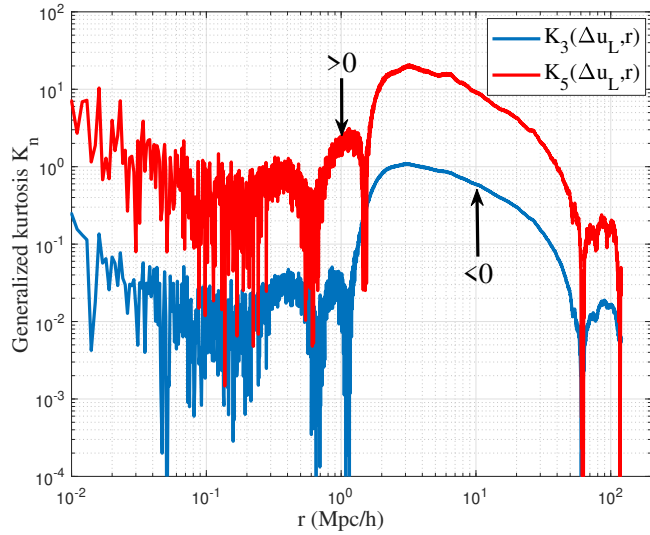


Figure 6. The odd-order generalized kurtosis of pairwise velocity Δu_L varying with scale r at $z=0$. The third order kurtosis $K_3(\Delta u_L, r)$ (skewness) vanishes on both small and large scales, where the distribution of Δu_L is symmetric. The skewness $K_3(\Delta u_L, r) < 0$ on the intermediate scale $r \approx r_t$ (distribution skews toward positive side). This negative skewness on the intermediate scale should be a result of an inverse cascade of kinetic energy from small to large scales up to the scale r_t of the largest haloes. The energy cascade on small scales $r < r_t$ [50] might also lead to the negative "effective" viscosity on large scales $r > r_t$ [6].

the simulation data reads

$$\langle \Delta u_L \rangle = -Har - ua^{-5/3} \left(\frac{r}{r_t} \right)^{5/2}, \quad (12)$$

where $u(a)$ is one-dimension velocity dispersion in Table 4.

On large scales, from the pair conservation Eq. (4), the mean pairwise velocity can be written as

$$\langle \Delta u_L \rangle \approx -\frac{2}{3}Har\bar{\xi}(r, a) = -\frac{2Ha}{r^2} \int_0^r \xi(y) y^2 dy. \quad (13)$$

With Eq. (87) for mean correlation $\bar{\xi}(r, a)$, the mean pairwise velocity is simply the derivative of the velocity correlation $R_2 = \langle \mathbf{u} \cdot \mathbf{u}' \rangle$ [see ref. 5, Eq. (124)]. Therefore, we should have

$$\langle \Delta u_L \rangle = \frac{2}{aHf(\Omega_m)} \frac{\partial R_2}{\partial r} = \frac{2a_0 u^2}{aHr_2} \exp\left(-\frac{r}{r_2}\right) \left(\frac{r}{r_2} - 4\right). \quad (14)$$

Figure 7 plots the mean longitudinal velocity $\langle u_L \rangle$ and pairwise velocity $-\langle \Delta u_L \rangle$ at different redshift z . Note that $\langle \Delta u_L \rangle = -2\langle u_L \rangle$ vanishes on both small and large scales. Since $\langle u_L \rangle = -\langle u'_L \rangle$, mean velocity sum $\langle \Sigma u_L \rangle = 0$ on all scales. Here, $\langle u_L \rangle > 0$ and $\langle \Delta u_L \rangle < 0$ reflect that two particles are moving toward each other due to gravity. In contrast, $\langle u_L \rangle = \langle \Delta u_L \rangle = \langle \Sigma u_L \rangle = 0$ on all scales for incompressible collisional hydrodynamics, where \mathbf{u} and \mathbf{r} are independent of each other. Models for pairwise velocity on small and large scales (Eqs. (12) and (14)) are also presented for comparison.

3.5 Second order moment of velocity

Figure 8 plots the second-order moments and the central moments (normalized by u_0^2) of velocities u_L , Δu_L , and Σu_L on all scales at $z=0$. Longitudinal velocities (u_L and u'_L) must be strongly correlated

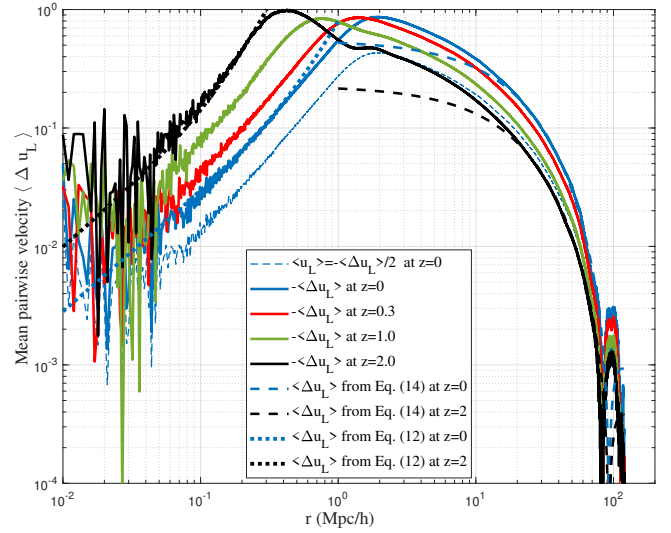


Figure 7. The variation of the mean (or first-order moment) longitudinal velocity $\langle u_L \rangle$ and mean pairwise velocity $|\langle \Delta u_L \rangle|$ with scale r at different redshifts z , normalized by velocity dispersion $u(a)$ in Table 4. Note that $\langle \Delta u_L \rangle = -2\langle u_L \rangle$ does not vanish on intermediate scale r_t and approaches zero on both small and large scales. The longitudinal velocity $\langle u_L \rangle = -\langle u'_L \rangle$ and the velocity sum $\langle \Sigma u_L \rangle = 0$ on all scales. For SG-CFD, the velocity field \mathbf{u} and vector \mathbf{r} between two particles are correlated leading to a nonzero longitudinal velocity $\langle u_L \rangle = \langle \mathbf{u} \cdot \mathbf{r} \rangle > 0$ on all scales.

on small scales due to gravitational interaction and uncorrelated on large scales. The correlation between u_L and u'_L leads to

$$\langle \Delta u_L^2 \rangle = 2\langle u_L^2 \rangle (1 - \rho_L), \quad \langle \Sigma u_L^2 \rangle = 2\langle u_L^2 \rangle (1 + \rho_L), \quad (15)$$

where ρ_L is the correlation coefficient. For small r and on small scales, $\rho_L = 1/2$ for $r \rightarrow 0$ [see ref. 5, Fig. 17]. Longitudinal velocities of particle pairs in small haloes are fully correlated with $\rho_L \rightarrow 1$, while the longitudinal velocities of particle pairs in large haloes are uncorrelated with $\rho_L \rightarrow 0$. Therefore, the average correlation is roughly $1/2$ [see ref. 5, Fig. 17]. From Eq. (15), on small scales with $\rho_L = 1/2$, we should have

$$\langle \Delta u_L^2 \rangle = \langle u_L^2 \rangle = \langle \Sigma u_L^2 \rangle / 3 = 2u^2. \quad (16)$$

On large scales with $\rho_L = 0$ when $r \rightarrow \infty$,

$$\langle \Delta u_L^2 \rangle = \langle \Sigma u_L^2 \rangle = 2\langle u_L^2 \rangle = 2u^2. \quad (17)$$

By contrast, for incompressible hydrodynamics, we have $\langle \Delta u_L^2 \rangle = 0$ and $\langle \Sigma u_L^2 \rangle = 4u^2$ on small scale with $\rho_L = 1$ when $r \rightarrow 0$, and $\langle u_L^2 \rangle = u^2$ on all scales (See comparison in Table 2).

The difference between the second-order moments and the central moments of u_L and Δu_L on intermediate scales is due to the nonzero first moments $\langle u_L \rangle$ and $\langle \Delta u_L \rangle$, as shown in Fig. 8 and Eq. (8). All second-order moments increase with r initially and decrease when $r > r_t$. The models for the second-order moment $\langle u_L^2 \rangle$ on small and large scales are presented in Eqs. (26) and (27).

Identifying all pairs of particles with different separation r , we can compute the velocity variance on different scales r , namely the total variance $\langle u^2 \rangle = \langle \mathbf{u} \cdot \mathbf{u} \rangle$, the longitudinal variance $\langle u_L^2 \rangle$ and the transverse variance $\langle u_T^2 \rangle = \langle \mathbf{u}_T \cdot \mathbf{u}_T \rangle$, where

$$\langle u^2 \rangle = \langle \mathbf{u} \cdot \mathbf{u} \rangle = \langle u_L^2 \rangle + \langle \mathbf{u}_T \cdot \mathbf{u}_T \rangle. \quad (18)$$

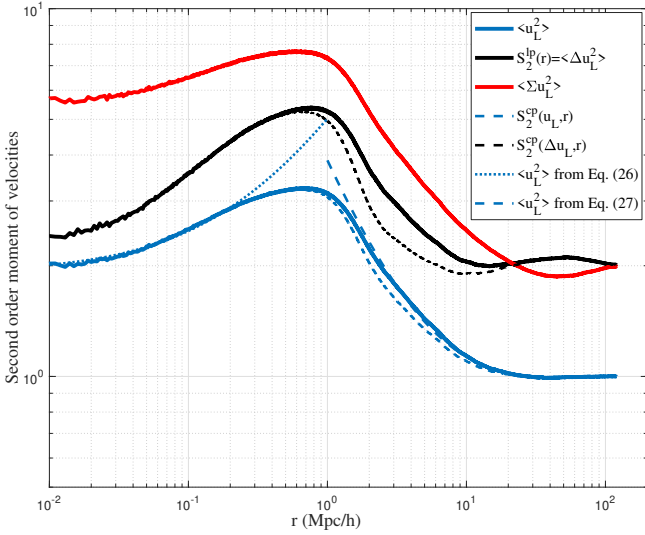


Figure 8. The variation of second-order moment $\langle u_L^2 \rangle$, $\langle \Delta u_L^2 \rangle$ and $\langle \Sigma u_L^2 \rangle$ with scale r at $z=0$, normalized by velocity dispersion u_0^2 of entire system in Table 4. On small scales, $\langle \Delta u_L^2 \rangle = \langle u_L^2 \rangle = \langle \Sigma u_L^2 \rangle / 3 = 2u^2$, while on large scales $\langle \Delta u_L^2 \rangle = \langle \Sigma u_L^2 \rangle = 2\langle u_L^2 \rangle = 2u^2$. The difference between the second-order longitudinal structure function $S_2^{lp}(r) = \langle \Delta u_L^2 \rangle$ and the central moment $S_2^{cp}(\Delta u_L, r)$ is due to the nonzero $\langle \Delta u_L \rangle$ on intermediate scales (Eq. (8)). On the contrary, $S_2^{lp} = S_2^{cp}$ and $\langle u_L^2 \rangle = u^2$ on all scales for incompressible hydrodynamics. Models for longitudinal velocity dispersion $\langle u_L^2 \rangle$ in Eq. (26) (small scales) and Eq. (27) (large scales) are also plotted.

Figure 9 plots three velocity dispersions $\langle u^2 \rangle$, $\langle u_L^2 \rangle$, and $\langle u_T^2 \rangle$ on different scale r at $z=0$. The initial increase of the three dispersions with r for $r < r_t$ (the pair of particles are more likely to be from the same haloes) is mostly due to the increase in the velocity dispersion with the size of the halo. With two particles forming a pair in Fig. 2 that are from different haloes on scale $r > r_t$, the velocity dispersions decrease sharply with r . At some large scale r , almost all pairs of particles are from different haloes, where velocity dispersions reach a plateau with $\langle u^2 \rangle = 3\langle u_L^2 \rangle = 3u^2$, where dispersion u^2 for all particles is listed in Table 4. The variation of $\langle u^2 \rangle$ can be related to the density correlation $\xi(r)$ through dynamic relations on large scales [see ref. 6, Eq. (120)]

For particle pairs separated by scale r , the second-order moments of longitudinal and transverse velocities are comparable on both small and large scales. However, $\langle u_L^2 \rangle > \langle u_T^2 \rangle / 2$ on intermediate scales with $\langle u_L^2 \rangle > \langle u^2 \rangle / 3$, that is, energy is not equipartition on intermediate scales. More kinetic energy is associated with the longitudinal velocity than with the transverse velocity. The velocity dispersion on small scales $\langle u_L^2 \rangle|_{r=0} \approx 2 \langle u_L^2 \rangle|_{r=\infty}$, i.e. the kinetic energy on small scales is twice the kinetic energy on large scales due to the finite velocity correlation $\rho_L = 1/2$ (Eqs. (16) and (17)).

The variation of pairwise velocity dispersion (or the second-order longitudinal structure function)

$$S_2^{lp} = \langle (\Delta u_L)^2 \rangle = \langle (u'_L - u_L)^2 \rangle$$

and the velocity sum

$$\langle (\Sigma u_L)^2 \rangle = \langle (u'_L + u_L)^2 \rangle$$

are also plotted in the same figure for comparison.

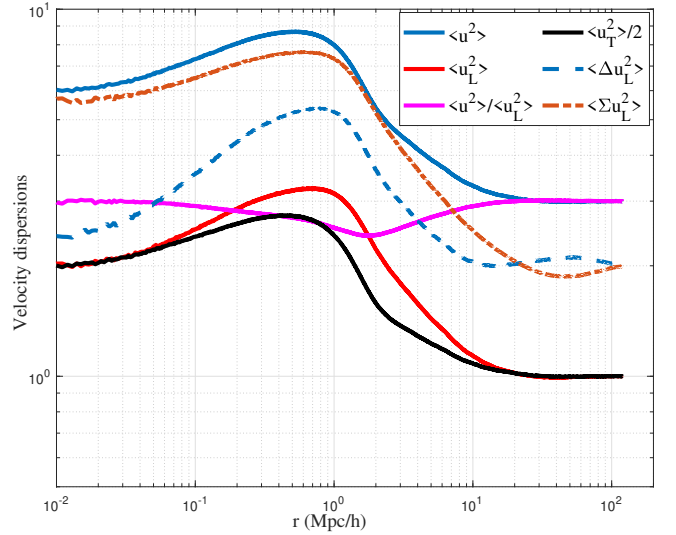


Figure 9. The variation of velocity dispersions $\langle u^2 \rangle = \langle \mathbf{u} \cdot \mathbf{u} \rangle$, $\langle u_L^2 \rangle$, and $\langle u_T^2 \rangle = \langle \mathbf{u}_T \cdot \mathbf{u}_T \rangle$ with scale r at $z=0$ (normalized by u_0^2). The initial increase of all dispersions with r for $r < r_t$ is mainly due to the increasing velocity dispersion with the size of the halo on small scales. With more pairs of particles from different haloes on larger scales $r > r_t$, the dispersion starts to decrease with r . With all pairs of particles from different haloes, the velocity dispersion reaches a plateau with $\langle u^2 \rangle = 3\langle u_L^2 \rangle = 3u^2$. The variation of $\langle u^2 \rangle$ can be related to the density correlation $\xi(r)$ through dynamic relations on large scales [see ref. 6, Eq. (120)].

3.6 Even order moments and two-thirds law

Now we focus on the second order structure function S_2^{lp} (pairwise velocity dispersion in Eqs. (9) and (19)) which is defined as

$$S_2^{lp}(r) = \langle (\Delta u_L)^2 \rangle = 2 \left(\langle u_L^2 \rangle - L_2(r) \right),$$

and a modified version of longitudinal structure function $S_2^l(r)$

$$S_2^l(r) = 2 \left(u^2 - L_2(r) \right).$$

With model for $\langle u_L^2 \rangle$ (Eq. (27)), model for $\langle u^2 \rangle$ [see ref. 6, Eq. (120)], and longitudinal correlation function $L_2 = \langle u_L u'_L \rangle$ [see ref. 5, Eq. (111)], structure functions $S_2^{lp}(r)$ and $S_2^l(r)$ on large sales can be completely modelled. On small scales, $S_2^l(r)$ was also determined to follow a one-fourth law $\propto r^{1/4}$ [see ref. 5, Eq. (137)]. However, the model for structure functions $S_2^{lp}(r)$ on small scales is still lacking.

Figure 10 presents the variation of the pairwise velocity dispersion $S_2^{lp}(r)$ with scale r and redshift z with limits $S_2^{lp}(r \rightarrow 0) = S_2^{lp}(r \rightarrow \infty) = 2u^2$ due to correlation coefficient $\rho_L = 1/2$ and $\rho_L = 0$ on small and large scales. Also, $S_2^{lp}(r) \approx S_2^l(r)$ for high redshift z , when the velocity distribution is nearly Gaussian, halo structures are not formed and $\langle u_L^2 \rangle \approx u^2$ on all scales (Eqs. (20) and (21)).

The two-thirds and four-fifths laws for second- and third-order structure functions in incompressible hydrodynamics in Eq. (1) are no longer valid for SG-CFD due to the collisionless nature of the flow. Since the peculiar velocity is of constant divergence on small scales [5], the second-order structure and correlation functions for the peculiar velocity should satisfy the same kinematic relations as if the peculiar velocity field is incompressible [5]. Furthermore, similarly to the direct energy cascade in 3D turbulence and the inverse energy cascade in 2D turbulence, there exists also a constant energy flux

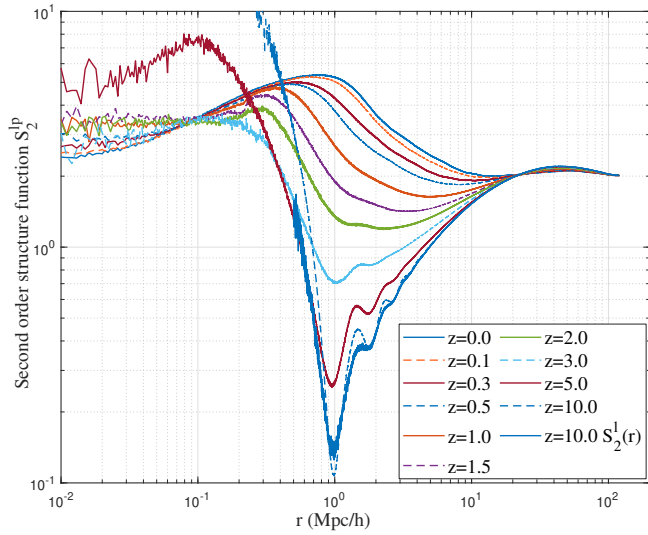


Figure 10. The variation of second order longitudinal structure function (or pairwise velocity dispersion) $S_2^{LP}(r)$ with scale r and redshifts z (normalized by velocity dispersion u^2 in Table 4). The two limits $S_2^{LP}(r \rightarrow 0) = S_2^{LP}(r \rightarrow \infty) = 2u^2$ due to correlation coefficient (between longitudinal velocities u_L and u'_L) $\rho_L = 1/2$ and $\rho_L = 0$ on small and large scales, respectively. Two second-order structure functions $S_2^{LP}(r) \approx S_2^I(r)$ at high redshift z ($z = 10$ in the figure) when velocity is still Gaussian and small scale structures are not developed (see Eqs. (20) and (21)).

$\varepsilon_u < 0$ in SG-CFD for the inverse kinetic energy cascade from small to large mass scales [25, 51]. Therefore, we expect that the second order structure function $S_2^{LP}(r)$ on small scales in SG-CFD should also be related to the constant energy flux ε_u in some way that is different from Eq. (1) for incompressible turbulence.

Since the viscous force is not present in SG-CFD, a reduced structure function $S_{2r}^{LP} = S_2^{LP} - 2u^2$ can be introduced with a vanishing limit $\lim_{r \rightarrow 0} S_{2r}^{LP} = 0$. The limiting pairwise velocity dispersion is inherent to all pairs of particles with $r \rightarrow 0$ and equals the kinetic energy on small scales, that is, $\lim_{r \rightarrow 0} S_2^{LP} = \lim_{r \rightarrow 0} \langle u_L^2 \rangle = 2u^2$. This part of kinetic energy reflects the collective motion of particles (the mean velocity of two particles) in the same halo that is not related to the energy cascade. Only the reduced structure function S_{2r}^{LP} reflects the excess pairwise velocity dispersion. This portion of kinetic energy is completely due to the random motion of particles of two particles that is relevant to the energy cascade [26]. This portion of the kinetic energy should be determined only by the constant energy flux ε_u (m^2/s^3) and the scale r . By a simple dimensional analysis, S_{2r}^{LP} must follow a two-thirds law, i.e., $S_{2r}^{LP} \propto (-\varepsilon_u)^{2/3} r^{2/3}$, which can also be derived from the scale independence of ε_u [50].

Here, to test this idea, Figure 11 plots the variation of reduced second-order structure function S_{2r}^{LP} with scale r at different redshifts z . A range with scaling $S_{2r}^{LP} \propto r^{2/3}$ can be clearly identified due to the formation of halo structures on small scales. This range gradually extends to larger scales due to the increasing critical scale r_t . The interesting finding is that the constant energy flux ε_u determines a new two-thirds law for a reduced second-order structure function S_{2r}^{LP} in SG-CFD. As expected, the reduced structure function quickly converges to $S_{2r}^{LP} \propto (-\varepsilon_u)^{2/3} r^{2/3}$ with the development of

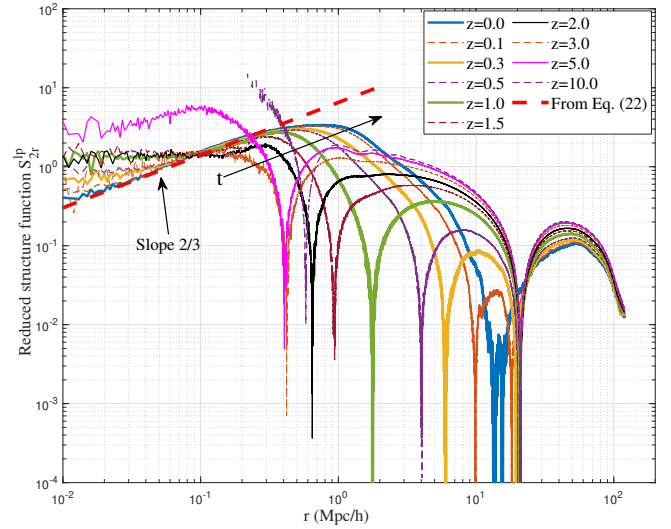


Figure 11. The variation of reduced longitudinal structure functions $S_{2r}^{LP} = (S_2^{LP} - 2u^2)$ with scale r at different redshifts z , normalized by velocity dispersion $u^2(a)$ in Table 4. A scaling of $S_{2r}^{LP} \propto (-\varepsilon_u)^{2/3} r^{2/3}$ (two-thirds law) can be clearly identified in a range that is gradually expanding with time, where $\varepsilon_u < 0$ is the constant rate of energy cascade. The model of Eq. (22) is also presented for comparison. When Combined with the structure formation and evolution in radiation and matter eras, this relation might be useful for postulating dark matter particle mass and properties on small scales [26].

halo structures. The length scale at which S_2^{LP} is at its maximum is approximately $r_d \approx 0.7aMpc/h$, the same as the length scale for $\langle u_L^2 \rangle$ [see ref. 5, Fig. 24].

Therefore, the second-order longitudinal structure function on small scales can be finally modeled as

$$S_{2r}^{LP}(r) = a^{3/2} \beta_2^* (-\varepsilon_u)^{2/3} r^{2/3},$$

$$S_2^{LP}(r) = u^2 \left[2 + \beta_2^* \left(\frac{r}{r_s} \right)^{2/3} \right] = 2u^2 + a^{3/2} \beta_2^* (-\varepsilon_u)^{2/3} r^{2/3}, \quad (22)$$

where the length scale r_s is purely determined by u_0 and ε_u with

$$r_s = -\frac{u_0^3}{\varepsilon_u} = \frac{4}{9} \frac{u_0}{H_0} = \frac{2}{3} u_0 t_0 \approx 1.58 Mpc/h, \quad (23)$$

which is roughly the scale below which the two-thirds law is valid. The rate of the energy cascade ε_u is estimated as

$$-\varepsilon_u = \frac{3}{2} \frac{u_0^2}{t_0} = \frac{9}{4} u_0^2 H_0 \approx 0.6345 \frac{u_0^3}{Mpc/h} = 4.6 \times 10^{-7} m^2/s^3, \quad (24)$$

where t_0 is the age of the universe (13.7 Billion years) [25, 51]. Constant $\beta_2^* \approx 9.5$ can be found from Fig. 11, where the model (22) is also presented for comparison.

With the model for $S_2^{LP}(r)$ in Eq. (22), Eq. (20), and model for longitudinal correlation $L_2(r)$ [see ref. 5, Eq. (138)],

$$L_2(r) = u^2 \left[1 - \left(\frac{r}{r_1} \right)^n \right], \quad (25)$$

the dispersion $\langle u_L^2 \rangle$ of longitudinal velocity (in Fig. 9) on small scales can be finally modeled as,

$$\langle u_L^2 \rangle = u^2 \left[2 - \left(\frac{r}{r_1} \right)^n + \frac{1}{2} \beta_2^* \left(\frac{r}{r_s} \right)^{2/3} \right], \quad (26)$$

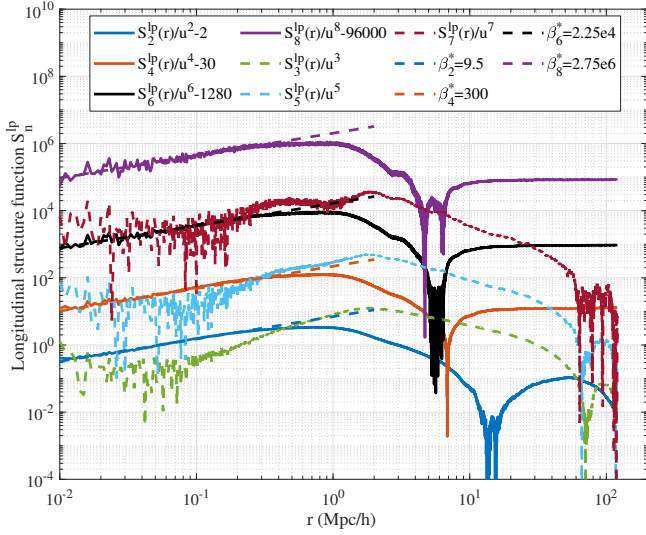


Figure 12. The variation of even and odd order structure functions with scale r at $z=0$. The plot demonstrates that even order **reduced** structure functions scales as $S_{2nr}^{lp} \propto \beta_{2n}^* r^{2/3}$ on small scales (Eq. (28)), while odd order structure functions scales as $S_{2n+1}^{lp} \propto r$. The numbers 2, 30, 1280... are related to the generalized kurtosis $K_{2n}(\Delta u_L, r)$ for the limiting distribution of pairwise velocity Δu_L when $r \rightarrow 0$ (Table 3).

where $n \approx 1/4$ and $r_1(a) \approx 19.4a^{-3} \text{ Mpc}/h$. While on large scales, the velocity dispersion $\langle u^2 \rangle$ can be related to the density correlation via dynamic relations [see ref. 6, Eq. (120)], the longitudinal velocity dispersion $\langle u_L^2 \rangle = \langle u^2 \rangle / 3$ reads

$$\langle u_L^2 \rangle = u^2 - \frac{2\nu}{3Hf(\Omega_m)^2} \frac{a_0 u^2}{rr_2} \cdot \exp\left(-\frac{r}{r_2}\right) \left[\left(\frac{r}{r_2}\right)^2 - 7\left(\frac{r}{r_2}\right) + 8 \right]. \quad (27)$$

where $\nu \approx -6000 \text{ Mpc}\cdot\text{km}/\text{s}$ is the negative effective viscosity at $z=0$ on large scales, $r_2 = 23 \text{ Mpc}/h$ is the characteristic scale for velocity correlations and the coefficient $a_0 = 0.45$ [see ref. 5, Fig. 21]. The negative effective viscosity reflects the inverse energy cascade [6]. The models for longitudinal velocity dispersion $\langle u_L^2 \rangle$ on small and large scales are plotted in Fig. 8.

Next, higher-order structure functions can be studied similarly. Figure 12 plots the variation of even and odd order structure functions $S_{2n+1}^{lp}(r)$ with scale r at $z=0$. It is now clear that the original Kolmogorov scaling (Eq. (1)) for incompressible flow does not apply to a self-gravitating collisionless dark matter flow due to the collisionless nature and long-range gravity. On small scales, all even order **reduced** structure functions follow $S_{2nr}^{lp} \propto \beta_{2n}^* r^{2/3}$, while all odd order structure functions follow a linear scaling such that $S_{2n+1}^{lp} \propto r$.

The general form for even order structure function $S_{2n}^{lp}(r)$ can be precisely modeled as,

$$S_{2n}^{lp}(r) = u^{2n} \left[2^n K_{2n}(\Delta u_L, r=0) + \beta_{2n}^* \left(\frac{r}{r_s}\right)^{2/3} \right], \quad (28)$$

where $K_{2n}(\Delta u_L, r=0)$ is the generalized kurtosis on the smallest scale that we can find from Fig. 5 (listed in Table 3 and modeled by

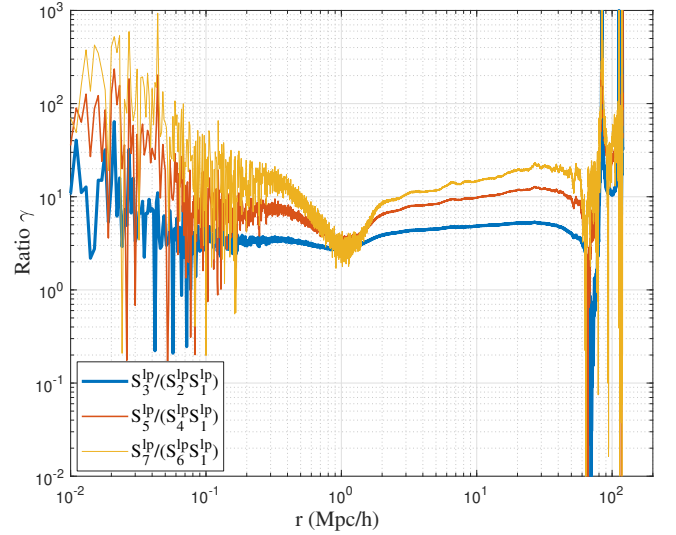


Figure 13. The variation of ratio $\gamma = S_{2n+1}^{lp}(r) / [S_1^{lp}(r) S_{2n}^{lp}(r)]$ for $n=1, 2$, and 3 with scale r at $z=0$. For $n=1$, this ratio is around three as predicted by the generalized stable clustering hypothesis (GSCH) [49].

Eq. (47)). The universal constants β_{2n}^* are determined as

$$\beta_2^* = 9.5, \quad \beta_4^* = 300, \quad \beta_6^* = 2.25 \times 10^4, \quad \beta_8^* = 2.75 \times 10^6, \quad (29)$$

or approximately

$$\beta_{2n}^* \approx 10^{1.826n-1.003}.$$

3.7 Odd order moments and stable clustering hypothesis

The mean pairwise velocity (first order moment) $S_1^{lp}(r) = \langle \Delta u_L \rangle = -Har$ on small scales (Fig. 7) can be obtained from the stable clustering hypothesis, which can be demonstrated by a two-body collapse model (TBCM) in an expanding background [49]. The same TBCM model can be extended to higher-order moments, i.e., the generalized stable clustering hypothesis, such that

$$S_{2n+1}^{lp}(r) = (2n+1) S_1^{lp}(r) S_{2n}^{lp}(r), \quad (30)$$

or $\gamma = S_{2n+1}^{lp} / [S_1^{lp} S_{2n}^{lp}] = (2n+1)$,

where γ is the ratio between odd and even order structure functions. From this, the odd-order structure functions can be written as:

$$S_{2n+1}^{lp}(r) = -2^n (2n+1) K_{2n}(\Delta u_L, r=0) Haru^{2n}. \quad (31)$$

Generalized kurtosis on the smallest scale $K_{2n}(\Delta u_L, r=0)$ is presented in the next section (Table 3 and Eq. (47)). With odd order moments in Fig. 12, Fig. 13 presents the ratio $S_{2n+1}^{lp}(r) / [S_1^{lp}(r) S_{2n}^{lp}(r)]$ for $n=1, 2$ and 3 at $z=0$. For $n=1$, this ratio is around three on small scales. For $n=2$ and 3 , this ratio slightly deviates from the predicted value of $(2n+1)$ with higher noise on small scales [49].

Finally, Table 2 presents a comprehensive comparison of the velocity field between incompressible hydrodynamics and self-gravitating collisionless dark matter flow (SG-CFD). The differences are due to the collisionless nature and long-range gravity in SG-CFD, where distributions of velocity are non-Gaussian on all scales. For incompressible flow, the direct energy cascade from large to small scales leads to negative skewness ($K_3=-0.4$) in the dissipation range. For SG-CFD, the inverse cascade from small to large scales leads to neg-

Table 2. Velocity fields in incompressible flow and SG-CFD

Quantity	Incompressible flow	Self-gravitating collisionless flow
$\langle u_L \rangle$	0 for all scale r	$\lim_{r \rightarrow 0, \infty} \langle u_L \rangle = 0$ varying with r
$\langle u_L^2 \rangle$	u^2 for all scale r	$\lim_{r \rightarrow 0} \langle u_L^2 \rangle = 2u^2$ $\lim_{r \rightarrow \infty} \langle u_L^2 \rangle = u^2$
$\langle u_L^3 \rangle$	0 for all scale r	$\lim_{r \rightarrow 0, \infty} \langle u_L^3 \rangle = 0$ varying with r
PDF of u_L	Gaussian	Non-Gaussian on all scales
Correlation ρ_L	$\lim_{r \rightarrow 0} \rho_L = 1$ $\lim_{r \rightarrow \infty} \rho_L = 0$	$\lim_{r \rightarrow 0} \rho_L = 1/2$ $\lim_{r \rightarrow \infty} \rho_L = 0$
$\langle \Delta u_L \rangle$	0 for all scale r	$\lim_{r \rightarrow 0, \infty} \langle \Delta u_L \rangle = 0$ varying with r
$\langle \Delta u_L^2 \rangle$	$\lim_{r \rightarrow 0} \langle \Delta u_L^2 \rangle = 0$ $\lim_{r \rightarrow \infty} \langle \Delta u_L^2 \rangle = 2u^2$	$\lim_{r \rightarrow 0} \langle \Delta u_L^2 \rangle = 2u^2$ $\lim_{r \rightarrow \infty} \langle \Delta u_L^2 \rangle = 2u^2$
$K_3(\Delta u_L)$	$\lim_{r \rightarrow 0} K_3(\Delta u_L) = -0.4$ $\lim_{r \rightarrow \infty} K_3(\Delta u_L) = 0$	$\lim_{r \rightarrow 0, \infty} K_3(\Delta u_L) = 0$ varying with r
$K_4(\Delta u_L)$	$\lim_{r \rightarrow 0} K_4(\Delta u_L) \approx 4$ $\lim_{r \rightarrow \infty} K_4(\Delta u_L) = 3$ (Gaussian)	$\lim_{r \rightarrow 0} K_4(\Delta u_L) = 7.5$ $\lim_{r \rightarrow \infty} K_4(\Delta u_L) = 4.2$
$\langle \Sigma u_L \rangle$	0 on all scales	0 on all scales
$\langle \Sigma u_L^2 \rangle$	$\lim_{r \rightarrow 0} \langle \Sigma u_L^2 \rangle = 4u^2$ $\lim_{r \rightarrow \infty} \langle \Sigma u_L^2 \rangle = 2u^2$	$\lim_{r \rightarrow 0} \langle \Sigma u_L^2 \rangle = 6u^2$ $\lim_{r \rightarrow \infty} \langle \Sigma u_L^2 \rangle = 2u^2$

ative skewness ($K_3 \approx -0.1$ to -1) around the intermediate scale r_t , while K_3 vanishes on both small and large scales (Fig. 6).

4 PROBABILITY DISTRIBUTIONS OF VELOCITY FIELD

4.1 Velocity distributions on small scales

On small scales, longitudinal velocities u_L and Σu_L should follow the same limiting distribution as $r \rightarrow 0$, which is different from the distribution of pairwise velocity Δu_L (Fig. 5). This section focuses on the probability distributions of u_L and Σu_L that should maximize the entropy of the system. In our previous work, based on the halo description of the self-gravitating collisionless system, u_L on small scales should follow a X distribution to maximize the entropy of the system. The X distribution simply reads [24]

$$X(v) = \frac{1}{2\alpha v_0} \frac{e^{-\sqrt{\alpha^2 + (v/v_0)^2}}}{K_1(\alpha)}, \quad (32)$$

where α is a shape parameter and $K_n(x)$ is the *modified* Bessel function of the second kind. The velocity scale v_0 satisfies

$$\alpha \frac{K_2(\alpha)}{K_1(\alpha)} v_0^2 = \langle u_L^2 \rangle, \quad (33)$$

where $\langle u_L^2 \rangle$ is the dispersion of velocity u_L in Fig. 8. It can be estimated that $v_0^2 \approx 0.84u_0^2$ with $\langle u_L^2 \rangle = 2.5u_0^2$ at $r=0.1$ Mpc/h (from Fig. 8) and $z=0$. With the shape parameter $\alpha \approx 1.33$ and $v_0^2 = 0.84u_0^2$, the X distribution is plotted in Fig. 14 for comparison with the distribution of u_L from N-body simulations. The velocity sum Σu_L should follow the same distribution but with a different variance, i.e., $\langle (\Sigma u_L)^2 \rangle \approx 3\langle u_L^2 \rangle$. All distributions are symmetric on small scales.

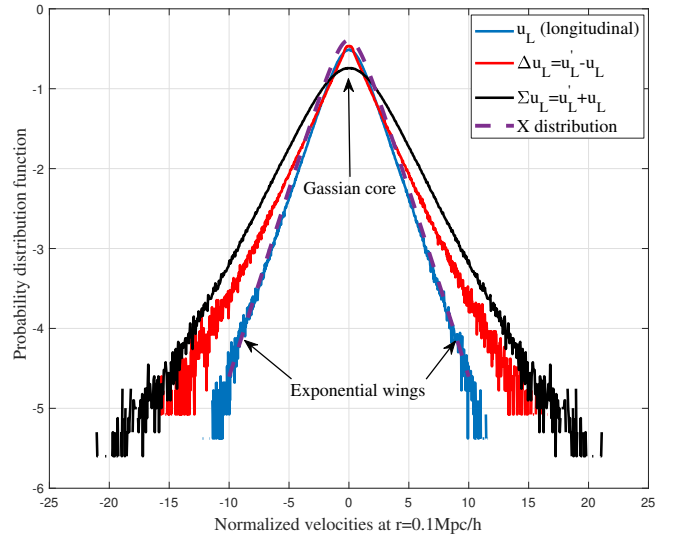


Figure 14. Probability Distributions of longitudinal velocity u_L , pairwise velocity Δu_L , and velocity sum Σu_L on a small scale of $r=0.1$ Mpc/h at $z=0$ from N-body simulations, i.e. $\log_{10} P$ vs. u_L/u_0 , where u_0 is the velocity dispersion at $z=0$ (Table 4). All distributions are symmetric with a vanishing skewness (third order kurtosis K_3). The X distribution that maximizes the system entropy (Eq. (32)) matches the distribution of u_L . Distributions have a Gaussian core for small velocity and exponential wings for large velocity. Velocity sum Σu_L also follows the X distribution but with a different variance. Pairwise velocity Δu_L follows a different distribution (Eq. (45)).

4.2 Distribution of pairwise velocity on small scales

The longitudinal velocity u_L has a finite limiting correlation $\rho_L = 1/2$ with $r \rightarrow 0$ such that the limiting distribution of the velocity difference (or pairwise velocity) Δu_L must be different from the distribution of u_L (Figs. 5 and 14). The longitudinal correlation depends on the size of the halo (Eq. (40)), where correlation approaches one in small haloes and zero in large haloes. This effect was not considered in previous work to determine the analytical distribution of Δu_L [52]. Again, the distribution of Δu_L on small scales cannot be Gaussian because of strong gravity (also see Fig. 5). The explicit form of that distribution is still unknown and should be explored in the future. However, in this section, the moments for the distribution of Δu_L can be rigorously estimated. This is also required to compute the generalized kurtosis in Eq. (28) for structure functions of pairwise velocity on small scales.

Let us start from an N-body system with a total of N collisionless particles. Figure 15 presents a schematic diagram of the halo picture by sorting all haloes in a system according to their sizes n_p from the smallest to the largest [24]. The halo size $n_p = m_h/m_p$, where m_h and m_p are the mass of the halo and single particle, respectively. Each column in Fig. 15 is a group of all haloes of the same size n_p . The total number of particles in a halo group reads

$$n_p N_h = N f(v) dv, \quad (34)$$

where N_h is the number of haloes in that halo group of size n_p , $f(v)$ is the dimensionless halo mass function with variable

$$v = \left(\frac{m_h}{m_h^*} \right)^{2/3} = \frac{\sigma_v^2}{\sigma_h^2}, \quad (35)$$

where m_h and m_h^* are the halo mass and the characteristic halo mass. Halo virial dispersion σ_v^2 is the dispersion of velocity of all particles

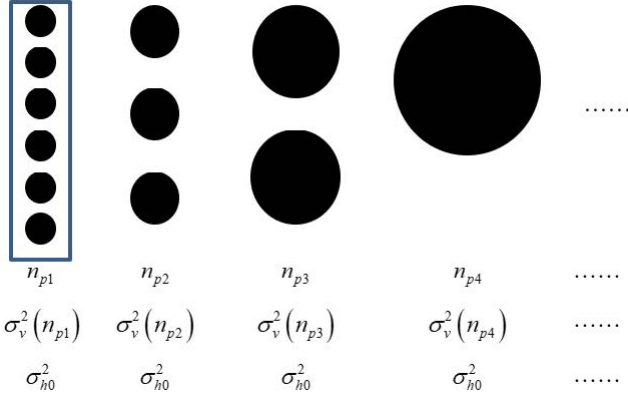


Figure 15. Schematic plot of groups of haloes of different sizes in an N -body system. All haloes are grouped and sorted according to the number of particles n_p in the halo, with size increasing from left to right. Every group of haloes of the same halo size, n_p , is characterized by the number of haloes in that group N_h , a halo virial dispersion $\sigma_v^2(n_p) \propto n_p^{2/3}$ increasing with halo size n_p , i.e. the dispersion of velocity of all particles in the same halo. The halo velocity dispersion (the dispersion of velocity of all haloes in the same group), $\sigma_h^2 = \sigma_{h0}^2$, is independent of halo size.

in the same halo and increases with halo size n_p . The halo velocity dispersion σ_h^2 is the dispersion of velocity of all haloes in the same group and is independent of halo size [24].

Let us assume that the number of particle pairs n_{pair} with a separation r in haloes of size n_p is proportional to the halo size n_p with a power law $n_{pair} = \mu_p (n_p)^{\alpha_p}$, where μ_p is a proportional constant. The larger haloes have more pairs of particles on a given scale r . The maximum number of pairs for a given halo size n_p is $n_{pair} = n_p (n_p - 1) / 2$ if all n_p particles collapse into a single point, where we have $\alpha_p = 2$. In principle, the exponent α_p satisfies $1 < \alpha_p < 2$. The number of pairs in a halo group (n_{pair}) reads

$$\begin{aligned} N_h n_{pair} &= N \mu_p (n_p)^{\alpha_p - 1} f(v) dv, \\ N_{pair} &= \int_0^\infty N \mu_p (n_p)^{\alpha_p - 1} f(v) dv. \end{aligned} \quad (36)$$

Here, N_{pair} is the total number of pairs with a given separation r in the entire N -body system.

From the virial theorem, the halo virial dispersion $\sigma_v^2 \propto (n_p)^{2/3}$ and we can write $n_p = \mu_v (\sigma_v^2 / \sigma_h^2)^{3/2}$, where μ_v is a proportional constant. Therefore, Eq. (36) can be transformed to

$$\frac{N_{pair}}{N \mu_p (\mu_v)^{\alpha_p - 1}} = \int_0^\infty f(v) v^{\frac{3}{2}(\alpha_p - 1)} dv, \quad (37)$$

or equivalently,

$$\int_0^\infty \beta_p f(v) v^p dv = 1,$$

where $\beta_p f(v) v^p dv$ is the fraction of pairs in a halo group with a given size n_p . Here, the exponent

$$p = 3(\alpha_p - 1) / 2. \quad (38)$$

Since the longitudinal velocity u_L for all particle pairs in the same halo group is nearly Gaussian [see ref. 24, Fig. 3], the distribution of pairwise velocity $\Delta u_L = u'_L - u_L$ can be obtained from the joint Gaussian distribution of u_L and u'_L with a size-dependent correlation

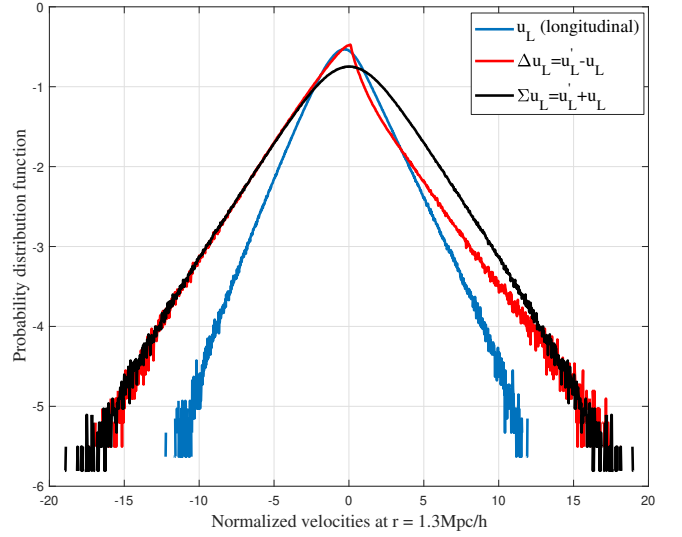


Figure 16. Distributions of u_L , Δu_L , and Σu_L on intermediate scales of $r = 1.3$ Mpc/h at $z=0$, i.e. $\log_{10} P_{uL}$ vs. u_L/u_0 , where u_0 is the velocity dispersion at $z = 0$ (Table 4). The distribution of Σu_L is symmetric, while the distribution of Δu_L is asymmetric with nonzero (negative) skewness (Fig. 18) and skew toward the positive side. This is a necessary feature of the inverse energy cascade. The distribution of u_L is also asymmetric with a nonzero mean and skewness.

coefficient $\rho_{cor}(n_p)$,

$$P_{\Delta uL}(x) = \int_0^\infty \frac{e^{-x^2/[4(1-\rho_{cor})\sigma^2]} \beta_p f(v) v^p dv}{\sqrt{2\pi} \sqrt{2(1-\rho_{cor})\sigma}}. \quad (39)$$

The correlation ρ_{cor} can be related to the total particle velocity dispersion σ^2 as [see ref. 5, Eq. (58)]

$$\rho_{cor}(n_p) = \sigma_h^2 / \sigma^2 \quad \text{and} \quad \sigma^2(n_p) = \sigma_v^2(n_p) + \sigma_h^2, \quad (40)$$

where σ_h^2 and σ_v^2 are the halo velocity dispersion and halo virial dispersion, respectively. For small haloes with $\sigma_v^2 \rightarrow 0$, the correlation coefficient $\rho_{cor} \rightarrow 1$. However, for large haloes with $\sigma_v^2 \rightarrow \infty$, the correlation coefficient $\rho_{cor} \rightarrow 0$. The size of the halo n_p is a function of the dimensionless variable v , that is, $n_p = \mu_v v^{3/2}$.

The moment generating function and the m th order moments can finally be obtained from Eq. (39),

$$\begin{aligned} \int_{-\infty}^\infty P_{\Delta uL}(x) e^{xt} dx &= \int_0^\infty \beta_p f(v) v^p e^{(1-\rho_{cor})\sigma^2 t^2} dv \\ &= \int_0^\infty \beta_p f(v) v^p e^{v \sigma_h^2 t^2} dv, \end{aligned} \quad (41)$$

$$M_m(\Delta u_L) = \frac{m!}{(m/2)!} \int_0^\infty \beta_p f(v) v^{p+m/2} dv \sigma_h^m. \quad (42)$$

We can use the double- λ mass function [see ref. 25, Eq. (21)] that is proposed based on the inverse mass cascade theory for hierarchical structure formation. The double- λ mass function $f(v)$ reads,

$$f(v) = f_{D\lambda}(v) = \frac{(2\sqrt{\eta_0})^{-q}}{\Gamma(q/2)} v^{q/2-1} \exp\left(-\frac{v}{4\eta_0}\right). \quad (43)$$

Here, the parameters $\eta_0 = 0.76$ and $q = 0.556$ for the best fit of the mass function to the simulation data. The normalization factor in Eq. (37) can be obtained as

$$\beta_p = \frac{N \mu_p (\mu_v)^{\alpha_p - 1}}{N_{pair}} = \frac{\Gamma(q/2)}{(2\sqrt{\eta_0})^{2p} \Gamma(p+q/2)}. \quad (44)$$

Table 3. Generalized kurtosis of velocity distributions on small and large scales from N-body simulations at $z=0$ and proposed models

Scale	Velocity	Distribution	4 th	6 th	8 th
$r \rightarrow 0$	$u_L, \Sigma u_L$	N-body, $z=0$, Fig. 5	4.8	57	1200
$r \rightarrow 0$	Δu_L	N-body, $z=0$, Fig. 5	7.5	160	6000
$r \rightarrow 0$	$u_L, \Sigma u_L$	X distribution (Eq. (32) $\alpha = 1.33$)	4.6	48.9	944.8
$r \rightarrow 0$	Δu_L	From model Eq. (47)	7.7	159.24	6356
$r \rightarrow \infty$	$\Delta u_L, \Sigma u_L$	N-body, $z=0$, Fig. 5	4.181	41.46	670.8
$r \rightarrow \infty$	u_L	N-body, $z=0$, Fig. 5	5.39	85.78	2800
Option 1					
$r \rightarrow \infty$	$\Delta u_L, \Sigma u_L$	Logistic (Eq. (49))	4.2	279/7	686
$r \rightarrow \infty$	u_L	$P_{uL}(x)$ (Eq. (52))	5.4	78.4	2270
Option 2					
$r \rightarrow \infty$	$\Delta u_L, \Sigma u_L$	X distribution (Eq. (32) $\alpha = 2.1$)	4.18	38.4	624
$r \rightarrow \infty$	u_L	$P_{uL}(x)$ (Eq. (52))	5.35	73.4	1936
		Laplace	6	90	2520
		Gaussian	3	15	105

Inserting the double- λ mass function into Eq. (41), the distribution of pairwise velocity $P_{\Delta u_L}$ satisfies (Eq. (41))

$$\int_{-\infty}^{\infty} P_{\Delta u_L}(x) e^{xt} dx = \frac{1}{(1 - 4\eta_0\sigma_h^2 t^2)^{p+q/2}}, \quad (45)$$

such that the moments of any order m can be obtained as,

$$M_m(\Delta u_L) = \frac{m! (2\sqrt{\eta_0})^m}{(m/2)! \Gamma(p+q/2)} \Gamma\left(\frac{1}{2}(m+2p+q)\right) \sigma_h^m. \quad (46)$$

The generalized kurtosis for pairwise velocity Δu_L is,

$$\bar{K}_{2n}(\Delta u_L) = \frac{(2n)! \Gamma(n+p+q/2) [\Gamma(p+q/2)]^{n-1}}{n! 2^n [\Gamma(1+p+q/2)]^n}, \quad (47)$$

where Kurtosis is completely determined by particle pair parameter p (Eq. (38)) and mass function parameter q (Eq. (43)). With $\eta_0 = 0.76$ and $q = 0.556$ for the double- λ mass function, $\beta_p \approx 1.5426$ from Eq. (44). Using the Kurtosis values for Δu_L on small scales from simulation (Table 3), the parameter $p \approx 0.36$ or exponent $\alpha_p \approx 1.24$ (from Eq. (38)) can be obtained. The total number of pairs N_{pair} with $r \rightarrow 0$ should be (from Eq. (44))

$$\frac{N_{pair}}{N} = \frac{\mu_p (\mu_v)^{\alpha_p - 1}}{\beta_p} \approx 0.26, \quad (48)$$

where both constants μ_p and μ_v can be obtained from simulation ($\mu_p \approx 0.21$ and $\mu_v \approx 14$ from the N-body simulation in Section 2 for particle pairs with a separation of $r=0.1\text{Mpc/h}$).

The general kurtosis for the distribution of pairwise velocity Δu_L on small scales can be calculated from Eq. (47) and listed in Table 3. The model agrees well with the N-body simulation. In addition, Table 3 lists the generalized kurtosis of three types of velocities on both small and large scales, both from models and from simulations. Again, the pairwise velocity Δu_L is usually approximated by an exponential (Laplace) distribution [52]. This seems not accurate, as the generalized kurtosis of the distribution of Δu_L from N-body simulations does not agree with that of the exponential distribution on both small and large scales (see Table 3).

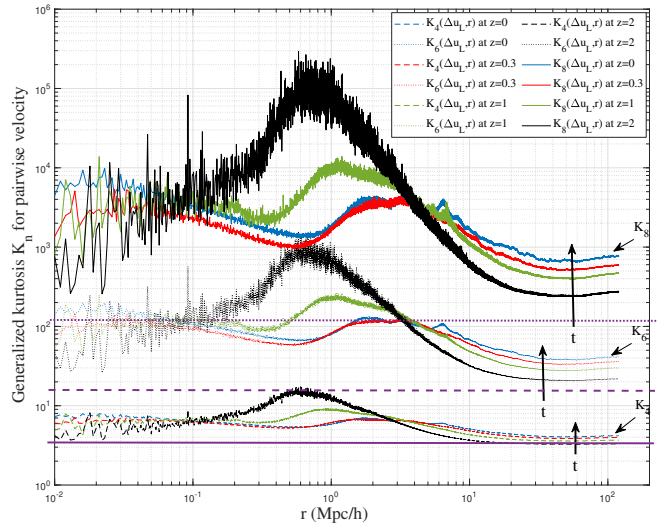


Figure 17. The redshift evolution of even order generalized kurtosis for pairwise velocity Δu_L at redshift $z = 2.0, 1.0, 0.3$, and 0 . The Kurtosis for the Gaussian distribution is also plotted for reference (purple lines). The distribution of Δu_L is non-Gaussian on all scales, while the evolution of the distribution on small scales is much faster than that on large scales due to the strong gravitational interaction on small scales (also see Fig. 21).

4.3 Velocity distributions on intermediate scales

Figure 16 presents the velocity distributions on an intermediate scale $r_t = 1.3\text{Mpc/h}$. The distributions of Δu_L and u_L are asymmetric with nonzero skewness (see K_3 in Fig. 18), which is due to the inverse cascade of kinetic energy from small scales to scale r_t (roughly the size of the largest haloes of characteristic mass m_h^*). The distribution of the velocity sum Σu_L is symmetric on all scales.

Figure 17 plots the redshift variation of generalized kurtosis K_4 , K_6 , and K_8 of pairwise velocity Δu_L at $z = 0, 0.3, 1$, and 2.0 . Kurtosis of the Gaussian distribution is also plotted for reference. All velocities are initially Gaussian. On small scales, most pairs of particles are from the same halo, and the distribution of the pairwise velocity Δu_L converges to the limiting distribution (Eq. (47)) much faster because of a strong intra-halo gravitational interaction. On large scales, the particle pairs are from different haloes. The distribution of Δu_L evolves slower because of the weaker inter-halo interaction at a greater distance. We revisit this in Fig. 21. Kurtosis on intermediate scales is much greater than that on both small and large scales.

Figure 18 plots the variation of K_3 (or skewness) of pairwise velocity Δu_L for $z = 0, 0.3, 1$, and 2.0 on small and intermediate scales. Skewness $K_3 \approx 0$ on small scales and $K_3 < 0$ on intermediate scales. Nonzero skewness is an important feature of the inverse energy cascade on small scales in the nonlinear regime.

4.4 Velocity distributions on large scales

On large scales, the velocities Δu_L and Σu_L have the same distribution as $r \rightarrow \infty$ (Fig. 5 and Table 3). The distribution of u_L at $r \rightarrow \infty$ has greater kurtosis than Δu_L and Σu_L . The non-Gaussian feature on large scales is a manifestation of the long-range nature of gravitational interaction. In contrast, velocity is always Gaussian on large scales for incompressible flow involving short-range interaction.

There seems to be no good theory for the distribution of pairwise velocity Δu_L on large scales, which is usually assumed to be expo-

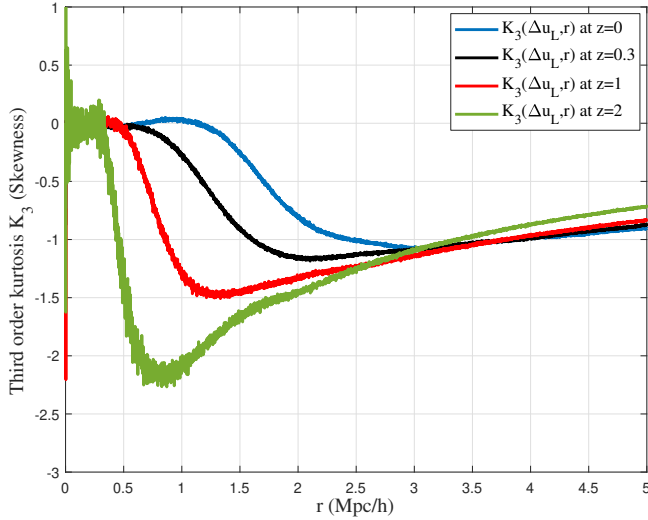


Figure 18. The redshift evolution of the skewness K_3 (third order generalized kurtosis) of Δu_L on intermediate scales. The skewness $K_3 \approx 0$ on small scales and $K_3 < 0$ on intermediate scales. A nonzero skewness is an important feature of inverse energy cascade on scales smaller than r_t , the size of the largest halo in Fig. 3. The minimum skewness increases with time, as does the critical scale r_t .

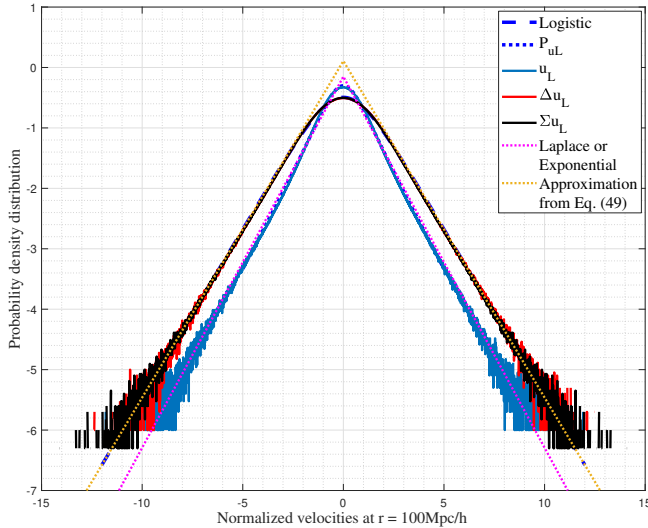


Figure 19. Distributions of u_L , Δu_L , and Σu_L on a large scale of $r = 100$ Mpc/h at $z=0$, i.e. $\log_{10} P_{uL}$ vs. u_L/u_0 (normalized by u_0). On large scales, all distributions are symmetric. Here, Δu_L and Σu_L follow the same distribution. A logistic distribution can be used to model the distribution of Δu_L and Σu_L . At large velocities, all distributions approach an exponential function. The longitudinal velocity u_L follows a different distribution that can be determined by the distribution of Σu_L (Eqs. (52) and (53)).

nential in the literature. However, the exponential distribution is not smooth and non-differentiable at zero velocity (Figs. 19 and 20). The kurtosis from the N-body simulation is not consistent with that of the exponential (or Laplace) distribution (Table 3). In this section, two options are proposed that are better than a non-smooth exponential distribution. Both options are listed in Table 3.

In the first option, a logistic distribution is proposed for both Δu_L

and Σu_L with a variance of $(s\pi)^2/3 = 2u^2$, where u^2 is the one-dimensional velocity dispersion of the entire N-body system (or the variance of u_L on large scales). The distribution reads

$$P_{\Delta u_L}(x) = \frac{1}{4s} \sec h^2\left(\frac{x}{2s}\right).$$

For large velocity x , the logistic distribution has exponential wing

$$P_{\Delta u_L}(x \rightarrow \infty) \approx \frac{1}{s} \exp\left(-\frac{x}{s}\right). \quad (49)$$

Assume P_{u_L} is the limiting distribution of u_L when $r \rightarrow \infty$. With correlation $\rho_L = 0$ at $r \rightarrow \infty$, the distribution of pairwise velocity Δu_L and longitudinal velocity u_L should satisfy the convolution

$$P_{\Delta u_L}(z) = \int_{-\infty}^{\infty} P_{u_L}(x) P_{u_L}(z-x) dx. \quad (50)$$

Using the characteristic function, the Fourier transform of two distributions satisfies

$$\hat{P}_{\Delta u_L}(t) = [\hat{P}_{u_L}(t)]^2. \quad (51)$$

For a logistic distribution for pairwise velocity Δu_L , the corresponding moment-generating function of u_L can be found from Eq. (51) with a variance of $(\pi s)^2/6 = u^2$,

$$MGF_{P_{u_L}}(t) = \hat{P}_{u_L} = \sqrt{\frac{\pi s t}{\sin(\pi s t)}}. \quad (52)$$

For the second option, the pairwise velocity Δu_L and the velocity sum Σu_L follow the X distribution on large scales. This is suggested by the N-body simulation (Table 3 and Fig. 21). Similarly, for this option, the distribution of Δu_L and corresponding moment-generating function of u_L are

$$P_{\Delta u_L}(x) = X(x) = \frac{1}{2\alpha v_0} \frac{e^{-\sqrt{\alpha^2 + (x/v_0)^2}}}{K_1(\alpha)}, \quad (53)$$

$$MGF_{P_{u_L}}(t) = \sqrt{\frac{K_1(\alpha\sqrt{1 + (v_0 t)^2})}{K_1(\alpha)\sqrt{1 + (v_0 t)^2}}}.$$

For both options, the explicit form of the distribution $P_{u_L}(x)$ is not available but can be obtained numerically from Eq. (52) or (53) using the inverse Fourier transform. The generalized kurtosis of u_L can be obtained directly from the moment-generating function for both options and presented in Table 3. The generalized kurtosis of the logistic distribution slightly agrees better with the simulation than the X distribution. The relevant distributions are also plotted in Figs. 19 and 20 and compared to the simulation with good agreement. All distributions are approximately exponential at high velocity.

4.5 Redshift evolution of velocity distributions

In this section, the redshift evolution of distributions of different types of velocities is presented. This includes the velocity u_p of all dark matter particles, the velocity u_{hp} of all halo particles, the velocity u_{op} of all out-of-halo particles, the velocity u_h of all haloes, and three types of longitudinal velocities u_L , Δu_L and Σu_L on both small and large scales, respectively. Since pairs of particles are from different haloes for a large scale r , the velocity u_{op} and u_h represent the velocity field on large scales. The velocity u_{hp} of all halo particles represents the velocity field on small scales. The redshift evolution of distributions of these velocities can be characterized by the redshift variation of the generalized kurtosis of these distributions.

If the evolution of a velocity always follows a family of X distributions with a shape parameter α that varies over time (Eq. (32)), the

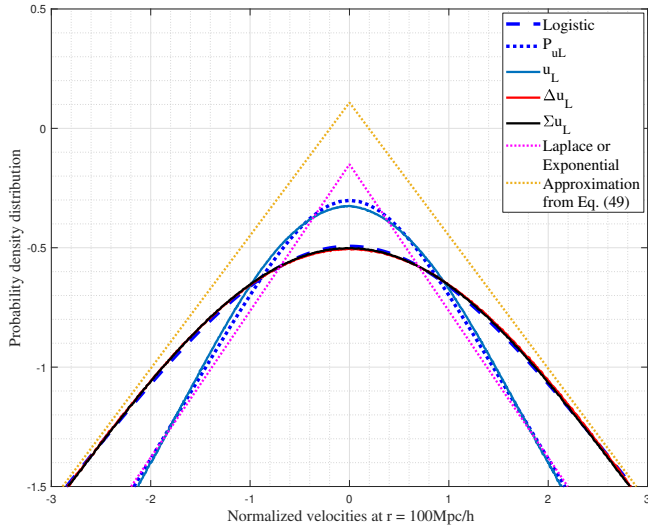


Figure 20. Comparison between proposed distributions with simulation data for small velocities. For pairwise velocity Δu_L , the logistic distribution shows better agreement with simulation data than the exponential distribution.

redshift evolution of the distribution of that velocity can be reduced to the redshift dependence of the shape parameter $\alpha \equiv \alpha(z)$. In this case, the redshift evolution of velocity distributions can be presented as the evolution of generalized kurtosis, which is a function of the redshift-dependent parameter $\alpha(z)$. The m th order kurtosis of the X distribution in Eq. (32) can be found as [see ref. 24, Table 2],

$$K_m(X) = \left(\frac{2K_1(\alpha)}{K_2(\alpha)} \right)^{m/2} \frac{\Gamma((1+m)/2)}{\sqrt{\pi}} \cdot \frac{K_{(1+m/2)}(\alpha)}{K_1(\alpha)}. \quad (54)$$

Figure 21 presents the redshift evolution of velocity distributions in terms of kurtosis of different order (4^{th} , 6^{th} , 8^{th} , and 10^{th}) from both the simulation (symbols) and Eq. (54) (gray lines). All velocities are initially Gaussian. With increasing time from left to right, all velocities become non-Gaussian, and the evolution approximately follows the prediction of the X distribution with decreasing α . The halo velocity (u_h), the out-of-halo particle velocity (u_{OP}), and the halo particle velocity (u_{HP}) should all follow a X distribution to maximize the system entropy, just as the longitudinal velocity u_L on small scales (Eq. (32)). The halo velocity (u_h) and the out-of-halo particle velocity (u_{OP}) follow similar distributions that evolve much slower than the evolution of the distribution of halo particle velocity (u_{HP}) because of stronger gravity on small scales. This is also consistent with the fact that virial equilibrium is established much faster for halo particles on small scales (owing to stronger gravity) than for the haloes themselves, which are on large scales.

The longitudinal velocity u_L and the velocity sum Σu_L follow the X distribution on small scales, while the pairwise velocity Δu_L follows the distribution given by Eq. (45). On large scales, the pairwise velocity Δu_L and the velocity sum Σu_L follows the X distribution approximately, while the longitudinal velocity u_L follows the distribution given by Eq. (53).

5 PROBABILITY DISTRIBUTIONS OF DENSITY FIELD

Various statistical measures can be introduced to characterize the velocity field in self-gravitating collisionless flow [5, 6], i.e., the real-space correlation, dispersion and structure functions, and power

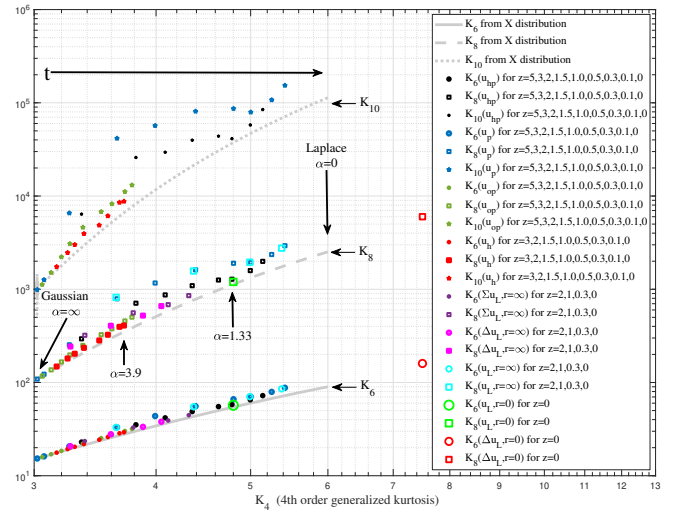


Figure 21. The variation of generalized kurtosis K_6 , K_8 , and K_{10} with K_4 for X distribution (gray lines) and for different types of velocities (symbols). In principle, the kurtosis of all different velocities increases with time, indicating the redshift evolution of velocity distributions to maximize the system entropy. These include the velocity u_p of all particles, the velocity u_{HP} of all halo particles, the velocity u_{OP} of all out-of-halo particles, and the velocity u_h of all haloes. By identifying the particle pairs on a given scale r , the distributions of the longitudinal velocity u_L , the pairwise velocity Δu_L , and the velocity sum Σu_L on small and large scales are also presented. All velocities are initially Gaussian with the shape parameter $\alpha = \infty$ and gradually become non-Gaussian with decreasing α . The evolution (approximately) follows the prediction (gray lines) of the X distribution. The distributions of out-of-halo particles u_{OP} and the velocity of the halo u_h match each other and evolve at a much slower pace compared to the velocity of the halo particles u_{HP} .

spectrum functions in Fourier space. They are related to each other through the kinematic and dynamic relations. The real-space correlation functions are the most fundamental quantity and building blocks of statistical theory. This section extends the statistical approach for the velocity field to the density field. Analytical models are also presented while available.

5.1 One-point probability distributions

Projecting a particle field onto a structured grid usually involves information loss and numerical noise. Without projecting onto the grid, Delaunay tessellation is used in this section to reconstruct the density field and to maximally preserve the information from the N -body simulation data. For a particle at location \mathbf{x} , the particle overdensity $\delta(\mathbf{x})$ and log-density $\eta(\mathbf{x})$ are defined as

$$\delta(\mathbf{x}) = \frac{\rho(\mathbf{x})}{\rho_0} - 1, \quad \eta(\mathbf{x}) = \log(1 + \delta(\mathbf{x})) = \log\left(\frac{\rho(\mathbf{x})}{\rho_0}\right), \quad (55)$$

where $\rho(\mathbf{x}) = m_p/V_p$ is a local matter density at comoving coordinate \mathbf{x} , m_p is the particle mass, V_p is the volume occupied by that particle, and ρ_0 is the mean (comoving) density. In linear theory, $\eta(\mathbf{x}) \approx \delta(\mathbf{x})$ for small overdensity $\delta(\mathbf{x}) \ll 1$ on large scales. They are different on small scales in the non-linear regime. Due to the normalization that the total volume should be equal to the sum of all particle volume ($\Sigma V_p = V$), the redshift evolution of the distributions of δ and η should always satisfy

$$\left\langle \frac{1}{1 + \delta(\mathbf{x})} \right\rangle = 1 \quad \text{and} \quad \left\langle e^{-\eta(\mathbf{x})} \right\rangle = 1. \quad (56)$$

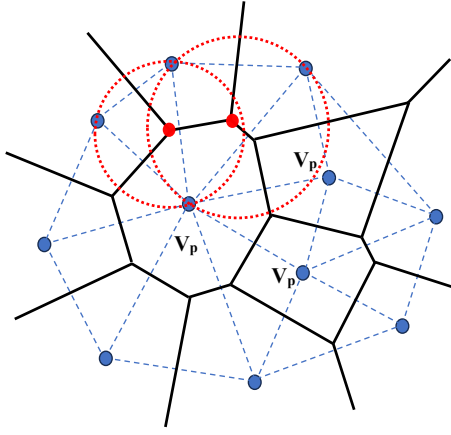


Figure 22. Schematic plot for the Delaunay tessellation in two-dimension to reconstruct the density field from a discrete set of particles. The first step is to connect all dark matter particles (blue dots) with a set of non-overlapping triangles (dashed lines). The second step is to find the circumcenter (red dots) of each triangle and connect them to form polygons (black solid lines). In two-dimension, the volume V_P that each dark matter particle occupies can be determined from the area of the polygon it resides in. The density of each particle can be calculated from the particle volume V_P .

Different from the velocity field, particle density is not a field variable that is automatically computed for every particle in an N-body simulation. Delaunay tessellation can be applied to reconstruct the density field from a discrete set of particles [53, 54]. Figure 22 presents a brief description of Delaunay tessellation in two-dimension. Generalization to three-dimension should be straightforward. All particles in the system are first connected by a set of non-overlapping tetrahedral (triangles in two dimensions). The volume V_P that each particle occupies can be determined from the volume of its surrounding tetrahedral. The density $\rho(\mathbf{x})$ of each particle can be calculated from the particle volume V_P . This enables us to compute the density distribution for halo particles and out-of-halo particles, respectively.

By calculating the density for each particle, Fig. 23a presents the redshift evolution of the one-point density distribution $\delta(\mathbf{x})$ for all particles in the N-body system. Due to gravitational collapse on small scales, $\delta(\mathbf{x})$ evolves from an initial Gaussian (symmetric) at high redshift to a "double power law" distribution (asymmetric and highly skewed toward $\delta > 0$) at $z=0$ with a long tail $\propto \delta^{-3}$. The distribution is approximately $\propto \delta^{-1}$ for small δ .

For comparison, the density distribution can also be obtained by projecting particles onto the structured grid using the Cloud-in-Cell (CIC) scheme with a given grid size (Δx). The results of the grid-based density distributions for different grid sizes Δx are presented in Fig. 23b. An approximate scaling of $\propto \delta^{-2}$ is consistent with the literature [17]. For grid-based density, $\langle \delta \rangle = 0$. Due to the limit of grid resolution, the grid-based density is much smaller than the particle density directly obtained from Delaunay tessellation (thick solid blue line).

Similarly, Fig. 24 plots the redshift evolution of the log-density distribution $\eta(\mathbf{x})$ from $z=10$ to $z=0$. A bimodal distribution is gradually developed from an initial Gaussian distribution. The first peak corresponds to out-of-halo particles in the low-density region that do not belong to any haloes with $\langle \eta \rangle < 0$. The second peak comes from all halo particles in haloes with higher density and wider dispersion. While other better fittings are possible, a simple bimodal equation is

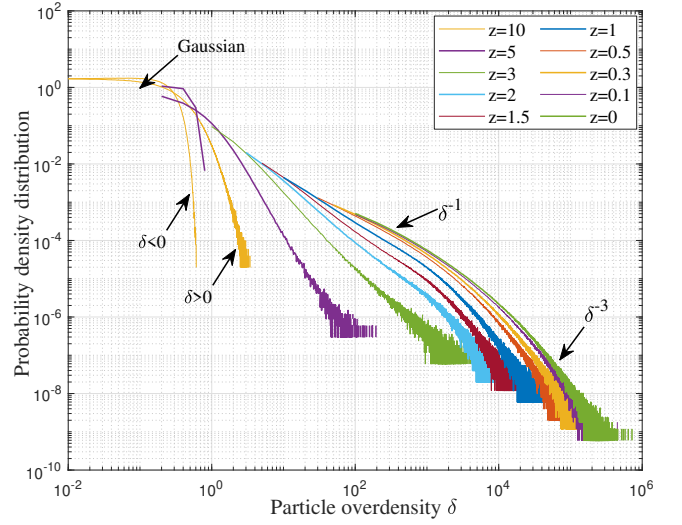


Figure 23a. The redshift evolution of the distribution of particle density δ from $z=10$ to $z=0$. Density evolves from an initial Gaussian distribution at high redshift with symmetric branches ($\delta > 0$ and $\delta < 0$) to a non-Gaussian distribution with a positive ($\delta > 0$) branch and a long tail $\propto \delta^{-3}$.

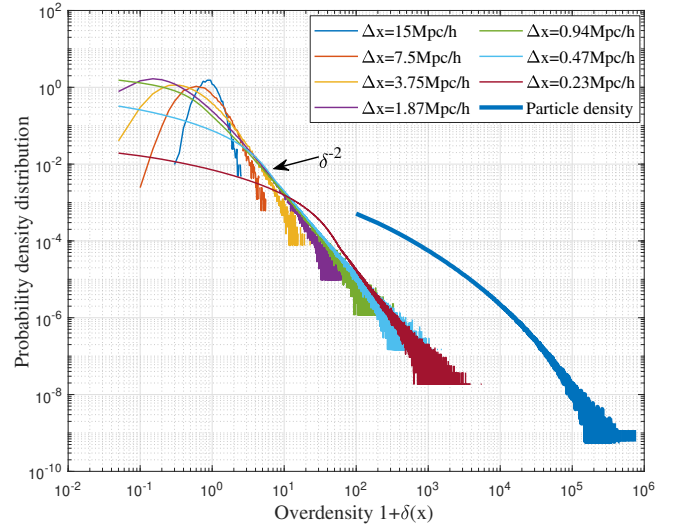


Figure 23b. The distribution of grid-based density ($1 + \delta$) obtained by projecting particles onto a structured grid of different grid size Δx at redshift $z=0$. On large scales (large Δx), the density distribution is Gaussian and symmetric. On small scales, the distribution extends to large density and becomes non-Gaussian with an approximate scaling of $\propto \delta^{-2}$. The particle density from Delaunay tessellation (corresponding to $\Delta x \rightarrow 0$) is also plotted for comparison that can reach greater density values than grid-based density.

used here to fit this distribution to provide additional insight,

$$f(\eta) = \frac{c_1}{\sqrt{2\pi}\sigma_1} \exp\left[-\frac{(\eta - \mu_1)^2}{2\sigma_1^2}\right] + \frac{1 - c_1}{\sqrt{2\pi}\sigma_2} \exp\left[-\frac{(\eta - \mu_2)^2}{2\sigma_2^2}\right] \quad (57)$$

with best fitting parameters $c_1 = 0.404$, $\mu_1 = -0.30$, $\sigma_1 = 1.212$, $\mu_2 = 4.256$, $\sigma_2 = 2.979$ at $z=0$. The fitted curve is plotted in the same figure with about 60% particles in haloes and 40% out-of-halo particles. This is consistent with the prediction from the inverse mass cascade [50], i.e., 60% of the total mass is in all haloes at $z = 0$.

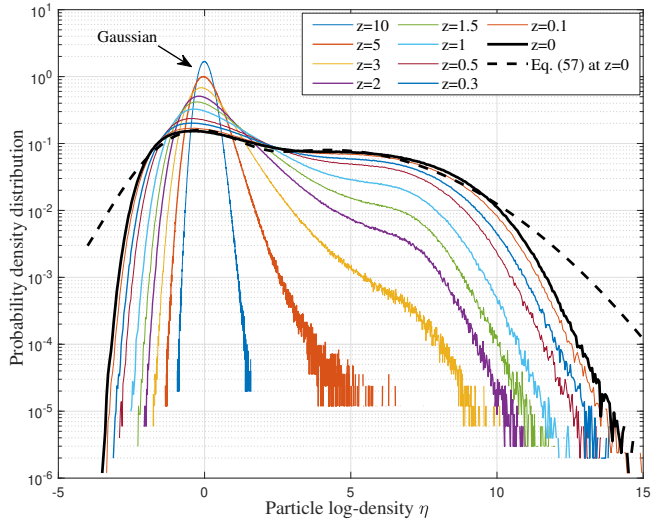


Figure 24. The distribution of the particle log-density $\eta(\mathbf{x})$ at different redshifts z . The log-density $\eta(\mathbf{x})$ evolves from a relatively Gaussian at high redshift to a bimodal distribution at $z=0$ with two peaks corresponding to halo (60%) and out-of-halo (40%) particles. Inverse mass cascade leads to continuous halo structure formation and the two peaks in density distribution.

There is a continuous injection of mass from the out-of-halo into the haloes as a result of the inverse mass cascade. The particles in haloes should have an average density close to $\delta = \Delta_c - 1$, where the critical density ratio $\Delta_c = 18\pi^2$ from a spherical collapse model or a two-body collapse model such that $\langle \eta \rangle \approx 5.17$ (matches μ_2 , which is the mean density for all halo particles).

It is also natural to check the density distributions of halo particles and out-of-halo particles separately. By identifying all haloes in the entire system and dividing all particles into halo and out-of-halo particles, Fig. 25 presents the redshift evolution of the distributions of log-density $\eta(\mathbf{x})$ for the halo and out-of-halo particles, respectively. For out-of-halo particles, the distribution of η is Gaussian, with a mean density decreasing over time. The distribution of δ is approximately log-normal for out-of-halo particles or a log-normal density distribution on large scales [15]. However, for halo particles, the distribution is non-Gaussian and evolves with increasing mean density as a result of the formation and growth of haloes. A peak develops around $\eta = 5$ at $z=0$ corresponding to the critical density ratio $\Delta_c = 18\pi^2$ for haloes.

Similarly to the velocity field, to characterize the redshift evolution of the distribution of any random variable τ , statistical quantities such as skewness and kurtosis should be used. A generalized kurtosis $K_n(\tau)$ for the variable τ is defined as

$$K_n(\tau) = \frac{\langle (\tau - \langle \tau \rangle)^n \rangle}{\langle (\tau - \langle \tau \rangle)^2 \rangle^{n/2}} = \frac{S_n^{cP}(\tau)}{S_2^{cP}(\tau)^{n/2}}, \quad (58)$$

where the central moment of order n for random variable τ reads

$$S_n^{cP}(\tau) = \langle (\tau - \langle \tau \rangle)^n \rangle. \quad (59)$$

The odd-order kurtosis should vanish for symmetric distributions. Specifically for Gaussian distribution, $K_3 = K_5 = 0$, $K_2 = 1$, $K_4 = 3$, $K_6 = 15$, and $K_8 = 105$.

Figure 26 presents the redshift evolution of generalized kurtosis. For the density of out-of-halo particles, kurtosis ($K_3(\eta)$ to $K_6(\eta)$) is relatively independent of time. The distribution is relatively Gaussian with $K_4 \approx 3$ and $K_6 \approx 15$ at $z=0$, such that the distribution of δ

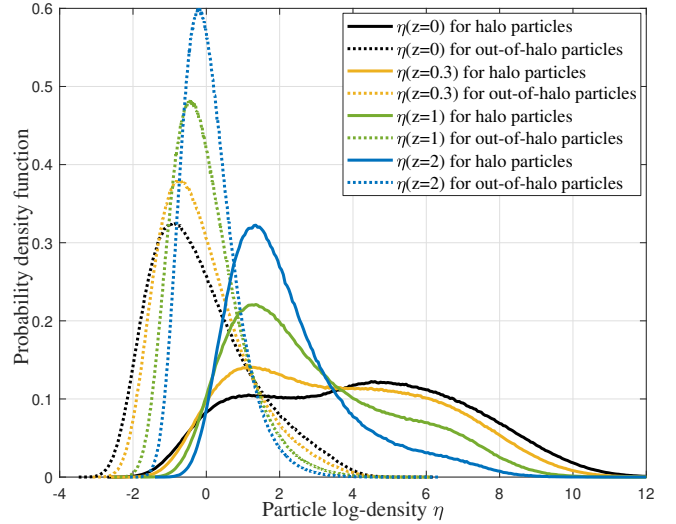


Figure 25. Redshift evolution of log-density distributions $\eta(z)$ for two different types of particles. For out-of-halo particles, the distribution is relatively Gaussian with a decreasing and negative mean density, with more and more out-of-halo particles forming haloes. This corresponds to a lognormal distribution of particle density $\delta(\mathbf{x})$ on large scales. For halo particles, the distribution evolves with an increasing mean log-density. A peak develops at around $\eta = 5$ corresponding to the critical density ratio $\Delta_c = 18\pi^2$.

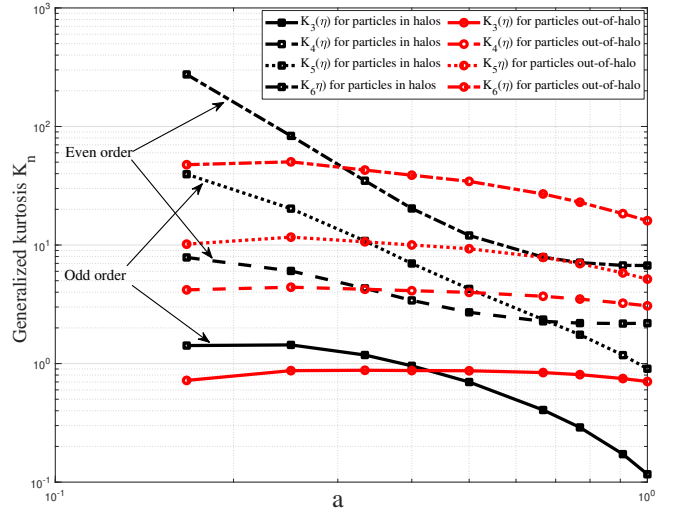


Figure 26. The redshift evolution of generalized kurtosis for distribution of log-density η for two different types of particles. The density distribution for the out-of-halo particles is relatively Gaussian with generalized kurtosis $K_4 \approx 3$ and $K_6 \approx 15$ at $z=0$. The density distribution for halo particles becomes more symmetric with vanishing odd-order kurtosis, while even-order kurtosis $K_4 \rightarrow 2$ and $K_6 \rightarrow 7$.

for out-of-halo particles is approximately log-normal. The density distribution of the halo particles approaches a symmetric distribution with odd-order kurtosis approaching zero and even-order kurtosis $K_4 \rightarrow 2$ and $K_6 \rightarrow 7$.

Figure 27 plots the variation in the mean and standard deviation of the log-density distribution with the scale factor a . For out-of-halo particles, the mean log-density decreases with time and $\langle \eta \rangle < 0$ after $z=1$ (or $a=0.5$). While the mean log-density of halo particles increases

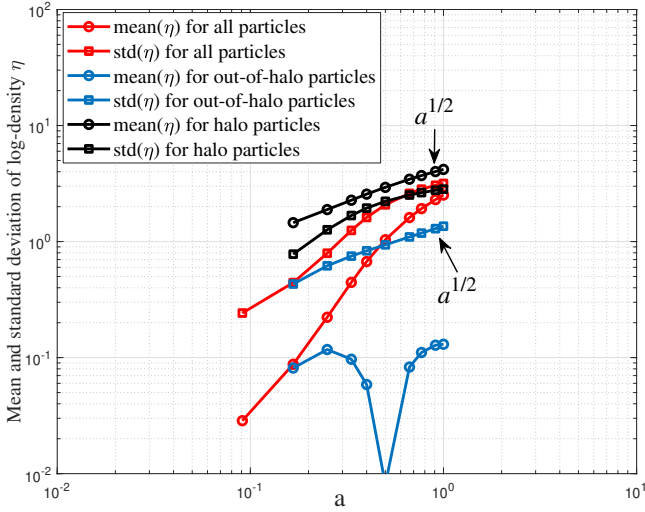


Figure 27. The variation of the mean and standard deviation of log-density $\eta(\mathbf{x}, z)$ with scale factor a . With more particles forming haloes and fewer out-of-halo particles, the mean log-density of out-of-halo particles decreases with time and $\langle \eta \rangle < 0$ after $z=1$. The mean log-density of all halo particles increases with time, and the standard deviation $std(\eta) \propto a^{1/2}$.

with time, i.e., $\langle \eta \rangle \propto a^{1/2}$. The power-law scaling of $std(\eta) \propto a^{1/2}$ can also be found for both halo and out-of-halo particles, reflecting the spreading of particle density due to continuous mass accretion. With more particles forming haloes and fewer out-of-halo particles, the density of out-of-halo particles extends to lower values. In contrast, the density of halo particles extends to higher values.

5.2 Two-point second-order statistical measures

5.2.1 Density correlation from radial distribution function

The gravitational interaction between collisionless particles leads to correlations in the position of the particles. Following the statistical mechanics of the molecular liquid, we start with the radial distribution function $g(r)$. This quantity is used to measure the average particle density around an arbitrary reference particle. The number of particles in the spherical shell of thickness dr at a distance r from the reference particle can be written as:

$$dN_p = g(r) \frac{N_p}{V} 4\pi r^2 dr, \quad (60)$$

where N_p/V is the mean density of particles, N_p is the total number of particles in the system, and V is the volume. The mean comoving density $\rho_0 = N_p m_p / V$. The normalization condition reads

$$\int_0^\infty g(r) 4\pi r^2 dr = \frac{N_p - 1}{N_p} V. \quad (61)$$

The two-point second order density correlation function is given by $\xi(r)$ that is related to the radial distribution function $g(r)$ as

$$\xi(r) = \langle \delta(\mathbf{x}) \delta(\mathbf{x} + \mathbf{r}) \rangle = g(r) - 1. \quad (62)$$

The normalization condition for density correlation reads (Eq. (61))

$$\int_0^\infty \xi(r, z) 4\pi r^2 dr = -V/N_p < 0. \quad (63)$$

Here, we find that the redshift-dependent density correlation $\xi(r, z)$ cannot be positive on all scales at any given time. Density must be negatively correlated on some scales.

Two length scales can be defined from the moments of density correlation (see Fig. 28),

$$l_{\delta 0}(a) = \int_0^\infty \xi(r, z) dr, \quad l_{\delta 1}^2(a) = \int_0^\infty \xi(r, z) r dr. \quad (64)$$

5.2.2 Potential and kinetic energy from density correlation

In principle, the specific potential energy (per mass) of any system with particles interacting via a pairwise potential $V_g(r)$ can be related to the radial distribution function $g(r)$ as

$$PE = \frac{2\pi\rho_0}{m_p^2} \int_0^\infty r^2 [g(r) - 1] V_g(r) dr, \quad (65)$$

where ρ_0 is the mean density. With $V_g(r) = -Gm_p^2/r$ for gravity, the specific potential energy of any N-body system reads

$$P_y(a) = -\frac{2\pi G\rho_0}{a} \int_0^\infty \xi(r, a) r dr = -\frac{3H_0^2 l_{\delta 1}^2}{4a} < 0. \quad (66)$$

The specific kinetic energy of the entire system can be related to the potential energy via a cosmic energy equation [55, 56, 57, 58],

$$\frac{\partial (K_p + P_y)}{\partial t} + H(2K_p + P_y) = 0, \quad (67)$$

with an exact solution of

$$K_p = a^{-2} \int_0^a a P_y da - P_y. \quad (68)$$

Substituting Eq. (66) into (68), the specific kinetic energy can be related to the density correlation [59] and length scale $l_{\delta 1}$,

$$\begin{aligned} K_p &= \frac{3}{4} H_0^2 a^{-1} \left[\int_0^\infty \xi(r, z) r dr - a^{-1} \int_0^a \left(\int_0^\infty \xi(r, z) r dr \right) da \right] \\ &= \frac{3}{4} H_0^2 a^{-1} \left(l_{\delta 1}^2 - a^{-1} \int_0^a l_{\delta 1}^2 da \right). \end{aligned} \quad (69)$$

Based on the theory of energy cascade for self-gravitation collisionless flow (SG-CFD) [26], the kinetic energy should evolve linearly over time t . Therefore, the evolution of the kinetic and potential energy of an N-body system in an expanding background can be modeled by a power-law solution [25, 26],

$$K_p = -\varepsilon_u t \quad \text{and} \quad P_y = \frac{7}{5} \varepsilon_u t, \quad (70)$$

which exactly satisfies the cosmic energy equation (Eq. (67)). Here, the rate of energy cascade ε_u is a negative constant reflecting the inverse cascade from small to large scales (Fig. 3) such that

$$\varepsilon_u = -\frac{3}{2} \frac{\partial u^2}{\partial t} \approx -\frac{3}{2} \frac{u_0^2}{t_0} \approx -10^{-7} m^2/s^3. \quad (71)$$

The length scale $l_{\delta 1}^2$ may be related to the rate of energy cascade ε_u as (using Eqs. (66) and (70)),

$$l_{\delta 1}^2(a) = \int_0^\infty \xi(r, z) r dr = -\frac{56}{45} \frac{\varepsilon_u}{H_0^3} a^{5/2}. \quad (72)$$

Figure 28 presents the variation of two length scales from the N-body simulation (defined in Eq. (64)) with the scale factor a . Two comoving correlation lengths show a limiting scaling of $l_{\delta 0}(a) \propto a^{5/2}$ and $l_{\delta 1}(a) \propto a^{5/4}$. The specific potential energy computed by Eq. (66) using $l_{\delta 1}$ is in good agreement with the potential energy directly obtained from the simulation. Both have a limiting scaling of $P_y(a) \propto a^{3/2}$ (see Eq. (70)).

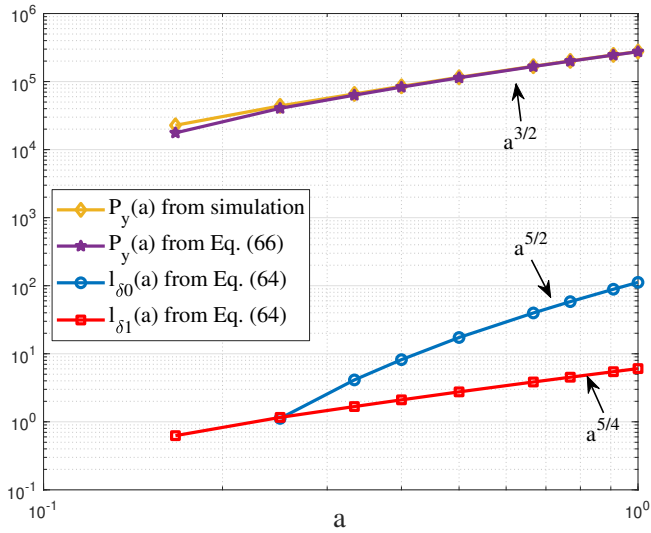


Figure 28. The variation of two correlation lengths $l_{\delta 0}(Mpc/h)$ and $l_{\delta 1}(Mpc/h)$ with the scale factor a . Both correlation lengths are derived from the density correlation $\xi(r, a)$ (Eq. (64)) with a limiting scaling $l_{\delta 1}(a) \propto a^{5/4}$ (Eq. (72)) and $l_{\delta 0}(a) \propto a^{5/2}$. The density correlation $\xi(r, z)$ from the N-body simulation is presented in Fig. 34. Potential energy $P_y(a)$ (in units of $(Km/s)^2$) using Eq. (66) is in good agreement with $P_y(a)$ which is directly computed from simulation, both of which show scaling of $P_y(a) \propto a^{3/2}$.

5.2.3 Density correlation, spectrum, and dispersion functions

Similarly to the statistical measures of the velocity field [5], in this section, we focus on the second-order statistical measures for the density field that can be directly obtained from the N-body simulation. Algorithms were developed to find all pairs of particles with a given separation r and compute the average of these statistical measures for all pairs with the same r . We first calculate the radial distribution function $g(r)$ (Eq. (60)) by counting the number of all pairs at a given distance of r . The density correlation can be obtained from $g(r)$ by Eq. (62). Using this approach, we avoid projecting a particle field onto the structured grid and maximally preserve information from the N-body simulation.

The density spectrum function $E_\delta(k, z)$ in the Fourier space can be obtained from the density correlation function $\xi(r, z)$. The density spectrum and correlation function are related through a pair of Fourier transformations:

$$E_\delta(k, z) = \frac{2}{\pi} \int_0^\infty \xi(r, z) kr \sin(kr) dr, \quad (73)$$

$$\xi(r, z) = \int_0^\infty E_\delta(k, z) \frac{\sin(kr)}{kr} dk. \quad (74)$$

In Peebles' convention [48], the matter power spectrum $P_\delta(k, z)$ is related to the density spectrum function as

$$P_\delta(k, z) = 2\pi^2 E_\delta(k, z) / k^2. \quad (75)$$

The dimensionless power spectrum $\Delta_\delta^2(k, z)$ (the power per logarithmic interval) can be related to the density spectrum as

$$\Delta_\delta^2(k, z) = E_\delta(k, z) k. \quad (76)$$

Figure 29 presents the density correlation $\xi(r, z)$ obtained for redshifts between $z=5$ and $z=0$. The correlation function on small scales

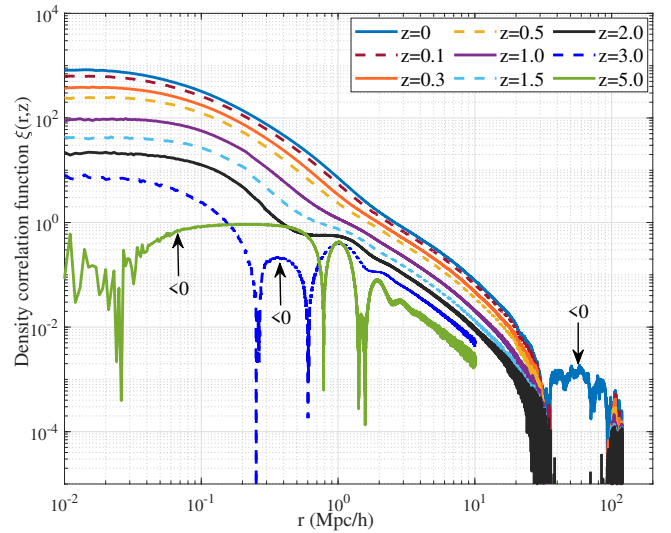


Figure 29. Two-point second order density correlation function $\xi(r, z)$ varying with scale r at different redshifts $z=0, 0.1, 0.3, 0.5, 1.0, 1.5, 2.0, 3.0$ and 5.0 . The density correlation turns negative at a fixed scale of around $33Mpc/h$. That scale is independent of the redshift (Eq. (86)) but can depend on the cosmology model. Since the mean density on a scale r is proportional to the density correlation on the same scale, i.e., $\langle \delta \rangle \propto \xi(r)$ [6], that scale also corresponds to the mean separation of cosmic voids with negative density.

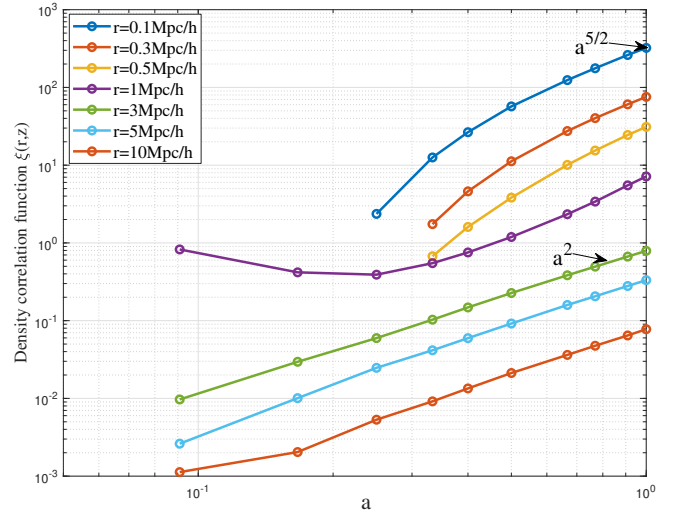


Figure 30. Two-point second order density correlation $\xi(r, z)$ varying with scale factor a on different scales $r = 0.1, 0.3, 0.5, 1.0, 3.0, 5.0$ and $10 Mpc/h$. The correlation $\xi(r, z) \propto a^2$ on large scales that are in the linear regime, and approximately $\propto a^{5/2}$ on small scales.

looks noisy at high redshifts ($z=3$ and $z=5$). There are a limited number of small-scale structures (haloes) at high redshift, which may lead to large fluctuations on small scales. The normalization condition in Eq. (63) requires negative density correlations on large scales. From the N-body simulation, the negative correlation $\xi(r, z) < 0$ can be found on scales greater than $33Mpc/h$ that is related to the critical scale r_2 for velocity correlations (Eq. (86)). Since the mean overdensity $\langle \delta \rangle$ is proportional to the density correlation on the same scale, that is, $\langle \delta \rangle \propto \langle \delta \delta' \rangle = \xi(r)$ [6], a negative correlation $\xi(r) < 0$ leads

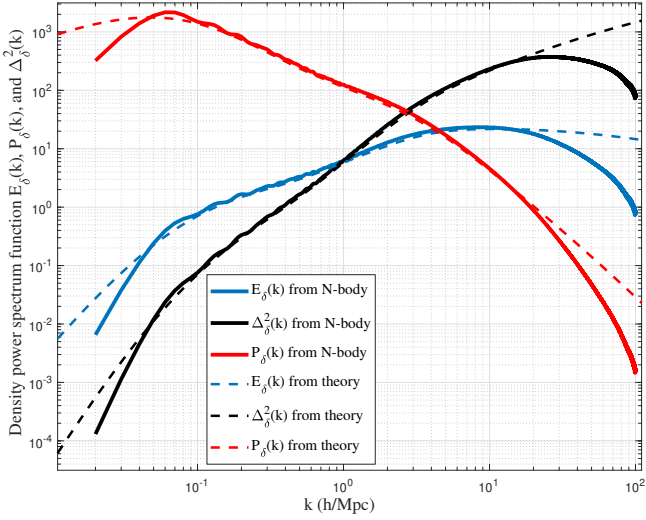


Figure 31. Without projecting particles onto a structured grid, density power spectrum $E_\delta(k)$ (Mpc/h), $P_\delta(k)$ (Mpc^3/h^3), and $\Delta_\delta^2(k)$ (dimensionless) can be obtained from correlation function $\xi(r)$ at $z=0$ in Fig. 29 by a Fourier transform. The nonlinear theory predictions (dashed lines) are also presented for comparison with good agreement. Model for $E_\delta(k)$ is presented in a separate paper [see ref. 5, Eq. (132)].

to a negative overdensity $\langle \delta \rangle < 0$ on the same scale corresponding to low-density cosmic voids on large scales.

Figure 30 plots the variation of $\xi(r, z)$ on a given scale r with the scale factor a . The density correlation follows the scaling $\xi(r, z) \propto a^2$ on large scales that is still in the linear regime ($r > r_t = 1Mpc/h$), while $\xi(r, a) \propto a^{5/2}$ on small scales in the nonlinear regime.

The power spectrum $E_\delta(k)$ can be obtained by a Fourier transform (Eq. (73)) of correlation function $\xi(r)$ that is directly obtained from the N-body simulations. Figure 31 presents three spectrum functions ($E_\delta(k)$, $P_\delta(k)$ from Eq. (75), and $\Delta_\delta^2(k)$ from Eq. (76)) at $z=0$. The prediction of nonlinear theory (dashed lines) is also presented for comparison [28] with good agreement with the spectrum function obtained from the correlation function $\xi(r)$. N-body simulation results are good for scales below the horizon scale. There are some discrepancies on scales beyond the horizon scale.

The variance of density fluctuations (density dispersion function), that is, the density fluctuation contained in all scales above r , reads

$$\sigma_\delta^2(r, z) = \int_{-\infty}^{\infty} E_\delta(k, z) W(kr)^2 dk, \quad (77)$$

where $W(x \equiv kr)$ is a window function when smoothed with a filter of size r . For a typical top-hat spherical filter, r is the radius of the filter, and the window function is written as

$$W(x) = \frac{3}{x^3} [\sin(x) - x \cos(x)] = 3 \frac{j_1(x)}{x}, \quad (78)$$

where

$$j_1(x) = \frac{\sin(x)}{x^2} - \frac{\cos(x)}{x} \quad (79)$$

is the *first* order spherical Bessel function of the first kind. With $W(0) = 1$, the variance of density fluctuation $\sigma_\delta^2(0) \rightarrow \infty$, i.e. diverging with $r \rightarrow 0$.

An exact relation between the correlation function $\xi(r)$ and the dispersion function $\sigma_\delta^2(r)$ for a top-hat filter in Eq. (78) can be

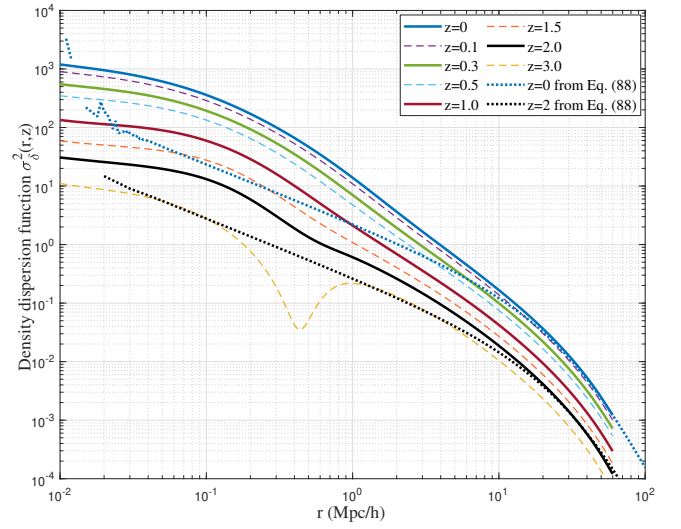


Figure 32. Density dispersion function $\sigma_\delta^2(r)$ at different redshift z obtained from density correlation $\xi(r)$ using Eq. (80). Density dispersions increase with time on all scales. Model from Eq. (88) is plotted for comparison with good agreement with simulation on large scales.

derived from Eqs. (74) and (77),

$$\xi(2r) = \frac{1}{72r^2} \frac{\partial}{\partial r} \left(\frac{1}{r^2} \frac{\partial}{\partial r} \left(r^3 \frac{\partial}{\partial r} \left(\sigma_\delta^2(r) r^4 \right) \right) \right). \quad (80)$$

For a power law density spectrum $E_\delta(k) \equiv bk^{-m}$, a power-law correlation is expected,

$$\xi(r) = -2b\Gamma(-m) \sin\left(\frac{m\pi}{2}\right) r^{m-1}, \quad (81)$$

along with a power-law density dispersion function

$$\sigma_\delta^2(r) = 72 \cdot 2^m b (1+m)(4+m) \Gamma(-5-m) \sin\left(\frac{m\pi}{2}\right) r^{m-1}. \quad (82)$$

It can be easily verified that Eqs. (81) and (82) satisfy Eq. (80).

The real space distribution of density fluctuations between scales $[r, r+dr]$ can be written as the derivative of density dispersion $\sigma_\delta^2(r)$

$$E_{\delta r}(r) = -\frac{\partial \sigma_\delta^2(r)}{\partial r}. \quad (83)$$

The function $E_{\delta r}$ represents the distribution of density fluctuations on scale r . This distribution can be related to the density spectrum function as (from Eqs. (77) and (83)),

$$E_{\delta r}(r) r^2 = -4 \int_0^\infty E_\delta\left(\frac{x}{r}\right) W(x) W'(x) x dx. \quad (84)$$

The distribution of density fluctuations $E_{\delta r}(r)$ contains the same information as the density spectrum in Fourier space. For a power law density spectrum, $E_\delta(k) \equiv bk^{-m}$, the fluctuation distribution $E_{\delta r}(r)$ can be exactly related to $E_\delta(k)$ as

$$E_{\delta r}(r) r^2 = E_\delta\left(\frac{x_0}{r}\right) \quad \text{and} \quad (85)$$

$$x_0 = \frac{1}{2} \left[-72 (m^2 - 1) (4+m) \Gamma(-5-m) \sin\left(\frac{m\pi}{2}\right) \right]^{-\frac{1}{m}}.$$

Finally, with the correlation function $\xi(r)$ fully determined from the simulation, we can translate it into the dispersion function $\sigma_\delta^2(r)$ via Eq. (80), the spectrum function E_δ via Eq. (73), and the real-space fluctuation distribution $E_{\delta r}(r)$ using Eq. (83).

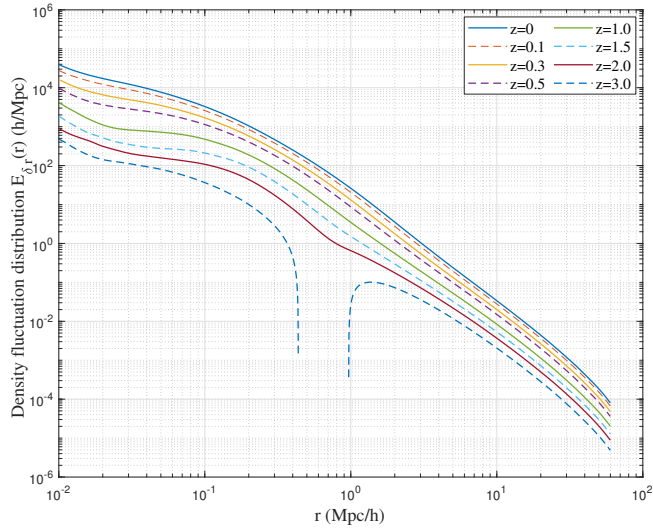


Figure 33. Real-space distribution of density fluctuation $E_{\delta r}(r)$ (h/Mpc) on scale r obtained from density dispersion function $\sigma_{\delta}^2(r)$ using Eq. (83). The density fluctuation increases with time on all scales, whereas the fluctuation on small scales increases faster than on large scales.

Figure 32 plots the variation of density dispersion $\sigma_{\delta}^2(r, z)$ at different redshifts obtained by integrating $\xi(r, z)$ (Eq. (80)) in Fig. 29, together with the model in Eq. (88) for comparison. Density dispersions increase with time on all scales. In particular, the commonly used σ_8^2 is a quantification of fluctuations in the density of matter on the scale $r=8Mpc/h$, that is, $\sigma_8^2 = \sigma_{\delta}^2(r=8Mpc/h)$ (see Fig. 34). Figure 33 presents the real space distribution of density fluctuations, that is, the function $E_{\delta r}(r)$, obtained from $\sigma_{\delta}^2(r)$ (Eq. (83)). Density fluctuations also increase with time on all scales.

Figure 34 presents the density correlation $\xi(r)$ at $z=0$ (solid blue curve). The density dispersion $\sigma_{\delta}^2(r)$ is obtained using Eq. (80) and plotted in solid purple with $\sigma_{\delta}^2(r=8Mpc/h) = \sigma_8^2$ that matches the simulation input in Table 1. The density correlation $\xi(r) < 0$ on scales greater than $33Mpc/h$, as required by normalization in Eq. (63). This negative correlation also means a negative mean overdensity (low-density voids) [6]. Linear (blue dashed line) and nonlinear theory prediction (red dashed line) are obtained by the Fourier transform of the model for the density spectrum function [28]. Note that both predictions underestimate the negative density correlation compared to the N-body results (blue solid). Models for $\xi(r)$ and $\sigma_{\delta}^2(r)$ (Eqs. (86) and (88)) are also plotted (dotted lines), which are consistent with the N-body simulation.

5.3 Models for second-order statistical measures

The density correlation on large scales can be analytically derived from the velocity correlation functions [see ref. 5, Section 5]. The exponential correlation for transverse velocity is a direct result of combined kinematics and dynamics on large scales [6], which leads to a simple form of density correlation [see ref. 5, Eq. (121)],

$$\xi(r, a) = \frac{a_0 u^2 / (r r_2)}{(a H f(\Omega_0))^2} \exp\left(-\frac{r}{r_2}\right) \left[\left(\frac{r}{r_2}\right)^2 - 7 \left(\frac{r}{r_2}\right) + 8 \right], \quad (86)$$

with parameter $a_0 u^2 = 0.45 u_0^2 a$ and $u^2(a)$ is the one-dimension velocity dispersion [see ref. 5, Fig. 21]. The values of a_0 and u at different redshift z are also listed in Table 4.

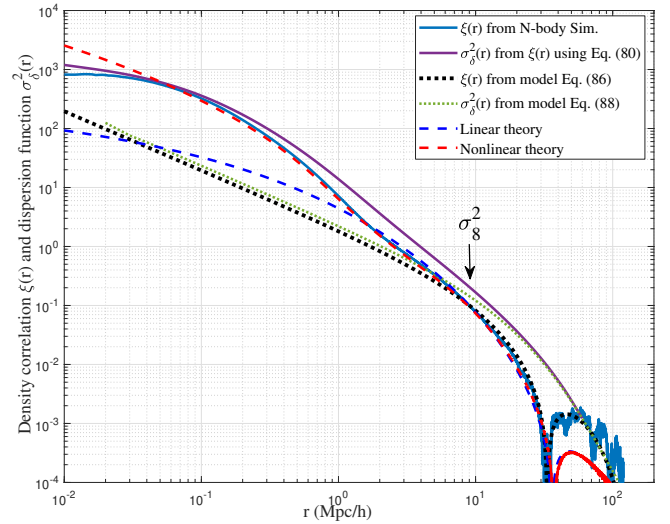


Figure 34. Two-point second order density correlation $\xi(r)$ (solid blue) and density dispersion $\sigma_{\delta}^2(r)$ (solid purple) varying with scale r at $z=0$. The negative density correlation can be identified for scales larger than $33Mpc/h$. Linear (blue dashed) and non-linear (red dashed) predictions are also presented in the same plot, and both underestimate the negative correlation on large scales. The dispersion function $\sigma_{\delta}^2(r)$ (solid purple) is obtained from Eq. (80). Models for $\xi(r)$ and $\sigma_{\delta}^2(r)$ (Eqs. (86) and (88)) are also presented in the same figure that captures the negative correlation.

Table 4. Parameters $a_0(z)$ and velocity dispersion $u(z)$ (km/s)

z	0	0.1	0.3	0.5	1.0	1.5	2.0	3.0
$a_0(z)$	0.451	0.463	0.486	0.509	0.559	0.604	0.643	0.694
$u(z)$	354.61	335.42	303.37	277.67	231.29	199.76	177.15	148.61

The only comoving length scale in this model $r_2 = 23.14Mpc/h$ is independent of the redshift. It is related to the size of the sound horizon and also dependent on the cosmology model [5]. Obviously $a_0 u^2 \propto a$ is consistent with the scaling $\xi(r, a) \propto a^2$ in linear theory. The density correlation turns negative at $0.5(7 - \sqrt{17})r_2 \approx 33Mpc/h$ according to Eq. (86). The model of Eq. (86) is also plotted in Fig. 34, which matches the N-body simulation on large scales.

The average correlation $\bar{\xi}(r, a)$ on large scales should read,

$$\begin{aligned} \bar{\xi}(r, a) &= \frac{3}{r^3} \int_0^r \xi(y, a) y^2 dy \\ &= \frac{a_0 u^2}{(a H f(\Omega_0))^2} \frac{3}{r r_2} \exp\left(-\frac{r}{r_2}\right) \left(4 - \frac{r}{r_2}\right), \end{aligned} \quad (87)$$

that can be related to the mean pairwise velocity via a pair conservation equation (Eq. (3)).

The density dispersion function $\sigma_{\delta}^2(r)$ for density fluctuations can be obtained using Eqs. (80) and (86),

$$\begin{aligned} \sigma_{\delta}^2(r) &= \frac{1}{(a H f(\Omega_0))^2} \cdot \frac{9 a_0 u^2}{2 r^2} \left\{ 3 \left(\frac{r_2}{r}\right)^4 + \left(\frac{r_2}{r}\right)^2 \right. \\ &\quad \left. - \exp\left(-\frac{2r}{r_2}\right) \left[1 + \left(\frac{r_2}{r}\right)^2 \right] \left[3 \left(\frac{r_2}{r}\right)^2 + 6 \left(\frac{r_2}{r}\right) + 4 \right] \right\}, \end{aligned} \quad (88)$$

where $\sigma_{\delta}^2(r) \propto a^2 r^{-4}$ for large $r \rightarrow \infty$ and $\sigma_{\delta}^2(r) \propto a^2 r^{-1}$ for $r \rightarrow 0$. The plots of the model are presented in Figs. 32 and 34.

6 CONCLUSIONS

Projecting the particle field onto a structured grid usually involves information loss and unnecessary noise. Without projecting the velocity and density fields, we introduce a new approach for the redshift and scale dependence of dark matter density and velocity distributions. By identifying all haloes in the entire N-body system and dividing all particles into halo particles and out-of-halo particles that do not belong to any haloes, and by computing the statistics over all pairs of particles on a given scale r , the scale and redshift variation of any statistical measures can be studied. This approach maximally preserves and utilizes the information from N-body simulations.

The scale dependence of the velocity field is studied for the longitudinal velocity u_L or u'_L , the velocity difference $\Delta u_L = u'_L - u_L$ (or the pairwise velocity) and the velocity sum $\Sigma u_L = u_L + u'_L$ (see Fig. 2). The fully developed velocity field is never Gaussian on any scale, despite the fact that they can initially be Gaussian (Figs. 4 and 5). In contrast, the velocity distribution is nearly Gaussian on large scales for incompressible hydrodynamics. The distribution of Σu_L approaches that of u_L on small scales with the correlation (between u_L and u'_L) $\rho_L \rightarrow 0.5$. On large scales, the distribution of Σu_L approaches that of Δu_L with correlation $\rho_L \rightarrow 0$.

Combining the pair conservation equation and density correlation, the first order moment of Δu_L (pairwise velocity) can be analytically modeled on small and large scales (Eqs. (12), (14) and Fig. 7). The second-order moment of three types of velocities is presented in Figs. 8 and 9, with an initial increase with scale r followed by a sharp decrease on the intermediate scales.

The second order moment of Δu_L , that is, the pairwise velocity dispersion $S_2^{lp}(r) = \langle (\Delta u_L)^2 \rangle$, approaches $2u^2$ on small scales (Fig. 10). A two-thirds law can be identified for a reduced structure function such that $S_{2r}^{lp} = (S_2^{lp} - 2u^2) \propto (-\varepsilon_u)^{2/3} r^{2/3}$ (Eq. (22) and Fig. 11), where ε_u is the constant rate of the energy cascade. The model for longitudinal velocity dispersion $\langle u_L^2 \rangle$ on small scales can be derived (Eq. (26) and Fig. 8). The two-thirds law can be generalized to all even-order structure functions $\langle (\Delta u_L)^{2n} \rangle$ (Eq. (28) and Fig. 12). In contrast, odd-order structure functions $\langle (\Delta u_L)^{2n+1} \rangle \propto r$ should satisfy the generalized stable clustering hypothesis (GSCH in Eq. (30) and Fig. 13). A complete comparison of velocity fields between incompressible flow and self-gravitating collisionless flow (SG-CFD) is listed in Table 2.

The distributions of three different velocities can be analytically modeled on small and large scales, respectively. On small scales, both the velocities u_L and Σu_L can be modeled by a X distribution to maximize system entropy (Fig. 14 and Eq. (32)). The explicit form for the distribution of Δu_L on small scales is still unknown. However, the moments and kurtosis of Δu_L can be analytically estimated (Eqs. (46) and (47)) using the joint Gaussian distribution with a size-dependent correlation coefficient ρ_{cor} (Eq. (39)). On intermediate scales, distributions of u_L and Δu_L become significantly nonsymmetric with nonzero skewness, a necessary feature of the inverse energy cascade. On large scales, both Δu_L and Σu_L approach the same distribution and can be modeled by a logistic function (Eq. (49) and Fig. 19) or X distribution. The distribution of u_L can also be obtained analytically in Eq. (51). The limiting distributions of different velocities on small and large scales are summarized in Table 3.

The redshift evolution of velocity distributions is summarized in Fig. 21. With time, all velocities become non-Gaussian, and the redshift evolution approximately follows the prediction of the X distribution with a decreasing parameter $\alpha(z)$ to continuously maximize the system entropy. However, the distribution of velocities on large

scales usually evolves much slower than the distribution of velocities on small scales because of stronger gravity on small scales.

For density distributions, Delaunay tessellation is used to reconstruct the comoving density field and maximally preserve information in the N-body simulation. The particle over-density δ evolves from an initial Gaussian to an asymmetric distribution with a long tail $\propto \delta^{-3}$ (Fig. 23a). The log-density η evolves from Gaussian to a bimodal distribution at $z=0$, with two peaks corresponding to the high density for halo particles and the low density for out-of-halo particles (Fig. 24). The log-density distribution for out-of-halo particles has a negative mean that decreases with time, while that for halo particles has an increasing mean (Fig. 27).

For density correlations, we first calculate the radial distribution function $g(r)$ for all scales r from the N-body simulation. The second order density correlation $\xi(r)$ can be obtained from $g(r)$ (Eq. (62)) and plotted in Figs. 34, 29, and 30. The density correlation cannot be positive on all scales due to normalization (Eq. (63)). The density spectrum E_δ and dispersion functions σ_δ^2 can be obtained from $\xi(r)$ using Eqs. (73) and (80), and presented in Figs. 34, 31, 32. The function $E_{\delta r}$ reflects the real-space distribution of the density fluctuations on different scales (Eq. (83) and Fig. 33) and contains the same information as the density spectrum E_δ (Eq. (84)). Analytical models for correlation and dispersion functions on large scales are also presented in Eqs. (86), (88), Figs. 34 and 32.

DATA AVAILABILITY

Two datasets underlying this article, that is, halo-based and correlation-based statistics of dark matter flow, are available on Zenodo [60, 61], along with the accompanying slides 'A comparative study of dark matter flow & hydrodynamic turbulence and its applications' [62]. All data files are also available on GitHub [63].

ACKNOWLEDGEMENTS

This research was supported by Laboratory Directed Research and Development at Pacific Northwest National Laboratory (PNNL). PNNL is a multiprogram national laboratory operated for the U.S. Department of Energy (DOE) by Battelle Memorial Institute under contract no. DE-AC05-76RL01830.

References

- [1] D. N. Spergel, L. Verde, H. V. Peiris, E. Komatsu, M. R. Nolta, C. L. Bennett, M. Halpern, G. Hinshaw, N. Jarosik, A. Kogut, M. Limon, S. S. Meyer, L. Page, G. S. Tucker, J. L. Weiland, E. Wollack, and E. L. Wright, *Seven-year Wilkinson Microwave Anisotropy Probe (WMAP) Observations* **148**, 175 (2003), arXiv:astro-ph/0302209 [astro-ph].
- [2] E. Komatsu, K. M. Smith, J. Dunkley, C. L. Bennett, B. Gold, G. Hinshaw, N. Jarosik, D. Larson, M. R. Nolta, L. Page, D. N. Spergel, M. Halpern, R. S. Hill, A. Kogut, M. Limon, S. S. Meyer, N. Odegard, G. S. Tucker, J. L. Weiland, E. Wollack, and E. L. Wright, *Astrophysical Journal Supplement Series* **192**, 18 (2011), arXiv:1001.4538 [astro-ph.CO].
- [3] N. Aghanim, Y. Akrami, M. Ashdown, J. Aumont, C. Baccigalupi, M. Ballardini, A. J. Banday, R. B. Barreiro, N. Bartolo, S. Basak, R. Battye, K. Benabed, J. P. Bernard, M. Bersanelli, P. Bielewicz, J. J. Bock, J. R. Bond, J. Borrill, F. R. Bouchet,

- F. Boulanger, M. Bucher, C. Burigana, R. C. Butler, E. Calabrese, J. F. Cardoso, J. Carron, A. Challinor, H. C. Chiang, J. Chluba, L. P. L. Colombo, C. Combet, D. Contreras, B. P. Crill, F. Cuttaia, P. de Bernardis, G. de Zotti, J. Delabrouille, J. M. Delouis, E. Di Valentino, J. M. Diego, O. Dore, M. Douspis, A. Ducout, X. Dupac, S. Dusini, G. Efstathiou, F. Elsner, T. A. Ensslin, H. K. Eriksen, Y. Fantaye, M. Farhang, J. Fergusson, R. Fernandez-Cobos, F. Finelli, F. Forastieri, M. Frailis, A. A. Fraisse, E. Franceschi, A. Frolov, S. Galeotta, S. Galli, K. Ganga, R. T. Genova-Santos, M. Gerbino, T. Ghosh, J. Gonzalez-Nuevo, K. M. Gorski, S. Gratton, A. Gruppuso, J. E. Gudmundsson, J. Hamann, W. Handley, F. K. Hansen, D. Herranz, S. R. Hildebrandt, E. Hivon, Z. Huang, A. H. Jaffe, W. C. Jones, A. Karakci, E. Keihanen, R. Keskitalo, K. Kiiveri, J. Kim, T. S. Kisner, L. Knox, N. Krachmalnicoff, M. Kunz, H. Kurki-Suonio, G. Lagache, J. M. Lamarre, A. Lasenby, M. Lattanzi, C. R. Lawrence, M. Le Jeune, P. Lemos, J. Lesgourgues, F. Levrier, A. Lewis, M. Liguori, *et al.*, *Astronomy & Astrophysics* **641**, A6 (2020), [arXiv:1807.06209](https://arxiv.org/abs/1807.06209) [astro-ph.CO].
- [4] Y. Z. Ma, M. Li, and P. He, *Astronomy & Astrophysics* **583** (2015), [10.1051/0004-6361/201526051](https://doi.org/10.1051/0004-6361/201526051).
- [5] Z. Xu, *Physics of Fluids* **35**, 0771105 (2023), [arXiv:2202.00910](https://arxiv.org/abs/2202.00910) [astro-ph].
- [6] Z. Xu, *Physics of Fluids* **36**, 075146 (2024), [arXiv:2202.02991](https://arxiv.org/abs/2202.02991) [astro-ph].
- [7] H. M. Courtois, A. Dupuy, D. Guinet, G. Baulieu, F. Ruppin, and P. Brenas, *A&A* **670**, L15 (2023), [arXiv:2211.16390](https://arxiv.org/abs/2211.16390) [astro-ph.CO].
- [8] R. Juszkiewicz, K. B. Fisher, and I. Szapudi, *The Astrophysical Journal* **504**, L1 (1998).
- [9] N. Seto, *The Astrophysical Journal* **520**, 409 (1999).
- [10] M. Davis and P. J. E. Peebles, *Astrophysical Journal Supplement Series* **34**, 425 (1977).
- [11] P. G. Ferreira, R. Juszkiewicz, H. A. Feldman, M. Davis, and A. H. Jaffe, *Astrophysical Journal* **515**, L1 (1999).
- [12] R. Juszkiewicz, P. G. Ferreira, H. A. Feldman, A. H. Jaffe, and M. Davis, *Science* **287**, 109 (2000).
- [13] K. Gorski, *Astrophysical Journal* **332**, L7 (1988).
- [14] K. M. Gorski, M. Davis, M. A. Strauss, S. D. M. White, and A. Yahil, *Astrophysical Journal* **344**, 1 (1989).
- [15] E. Hubble, *Astrophysical Journal* **79**, 8 (1934).
- [16] F. Bernardeau and L. Kofman, *Astrophysical Journal* **443**, 479 (1995).
- [17] A. Klypin, F. Prada, J. Betancort-Rijo, and F. D. Albareti, *Monthly Notices of the Royal Astronomical Society* **481**, 4588 (2018).
- [18] M. Kuhlen, N. Weiner, J. Diemand, P. Madau, B. Moore, D. Potter, J. Stadel, and M. Zemp, *Journal of Cosmology and Astroparticle Physics* (2010), [10.1088/1475-7516/2010/02/030](https://doi.org/10.1088/1475-7516/2010/02/030).
- [19] P. Ullio and M. Kamionkowski, *Journal of High Energy Physics* (2001), [10.1088/1126-6708/2001/03/049](https://doi.org/10.1088/1126-6708/2001/03/049).
- [20] Y. Zhao, X. J. Bi, P. F. Yin, and X. M. Zhang, *Physical Review D* **97**, 063013 (2018).
- [21] M. Petac, P. Ullio, and M. Valli, *Journal of Cosmology and Astroparticle Physics* (2018), [10.1088/1475-7516/2018/12/039](https://doi.org/10.1088/1475-7516/2018/12/039).
- [22] S. Kazantzidis, J. Magorrian, and B. Moore, *Astrophysical Journal* **601**, 37 (2004).
- [23] R. Wojtak, E. L. Lokas, G. A. Mamon, S. Gottlober, A. Klypin, and Y. Hoffman, *Monthly Notices of the Royal Astronomical Society* **388**, 815 (2008).
- [24] Z. Xu, *A&A* **675**, A92 (2023), [arXiv:2110.03126](https://arxiv.org/abs/2110.03126) [astro-ph].
- [25] Z. Xu, *Scientific Reports* **13**, 16531 (2023), [arXiv:2210.01200](https://arxiv.org/abs/2210.01200) [astro-ph].
- [26] Z. Xu, *arXiv e-prints*, [arXiv:2202.07240](https://arxiv.org/abs/2202.07240) (2022).
- [27] C. S. Frenk, J. M. Colberg, H. M. P. Couchman, G. Efstathiou, A. E. Evrard, A. Jenkins, T. J. MacFarland, B. Moore, J. A. Peacock, F. R. Pearce, P. A. Thomas, S. D. M. White, and N. Yoshida., [arXiv:astro-ph/0007362v1](https://arxiv.org/abs/astro-ph/0007362v1) (2000), [10.48550/arXiv.astro-ph/0007362](https://doi.org/10.48550/arXiv.astro-ph/0007362).
- [28] A. Jenkins, C. S. Frenk, F. R. Pearce, P. A. Thomas, J. M. Colberg, S. D. M. White, H. M. P. Couchman, J. A. Peacock, G. Efstathiou, and A. H. Nelson, *Astrophysical Journal* **499**, 20 (1998).
- [29] Z. Xu, *arXiv e-prints*, [arXiv:2201.12665](https://arxiv.org/abs/2201.12665) (2022).
- [30] R. E. Angulo, V. Springel, S. D. M. White, A. Jenkins, C. M. Baugh, and C. S. Frenk, *Monthly Notices of the Royal Astronomical Society* **426**, 2046 (2012).
- [31] V. Springel, *Monthly Notices of the Royal Astronomical Society* **364**, 1105 (2005).
- [32] P. J. E. Peebles, A. L. Melott, M. R. Holmes, and L. R. Jiang, *Astrophysical Journal* **345**, 108 (1989).
- [33] G. Efstathiou, M. Davis, C. S. Frenk, and S. D. M. White, *Astrophysical Journal Supplement Series* **57**, 241 (1985).
- [34] E. Jennings, C. M. Baugh, and S. Pascoli, *Monthly Notices of the Royal Astronomical Society* **410**, 2081 (2011).
- [35] O. Hahn, R. E. Angulo, and T. Abel, *Monthly Notices of the Royal Astronomical Society* **454**, 3920 (2015).
- [36] S. Pueblas and R. Scoccimarro, *Physical Review D* **80** (2009), [10.1103/PhysRevD.80.043504](https://doi.org/10.1103/PhysRevD.80.043504).
- [37] G. Jelic-Cizmek, F. Lepori, J. Adamek, and R. Durrer, *Journal of Cosmology and Astroparticle Physics* (2018), [10.1088/1475-7516/2018/09/006](https://doi.org/10.1088/1475-7516/2018/09/006).
- [38] R. W. Hockney and J. W. Eastwood, *Computer Simulation Using Particles* (Taylor & Francis, Bristol, PA, USA, 1988).
- [39] C. M. Baugh and G. Efstathiou, *Monthly Notices of the Royal Astronomical Society* **270**, 183 (1994).
- [40] C. M. Baugh, E. Gaztanaga, and G. Efstathiou, *Monthly Notices of the Royal Astronomical Society* **274**, 1049 (1995).
- [41] G. I. Taylor, *Proceedings of the royal society A* **151**, 421 (1935).
- [42] G. I. Taylor, *Proceedings of the Royal Society of London Series a-Mathematical and Physical Sciences* **164**, 0015 (1938).
- [43] T. de Karman and L. Howarth, *Proceedings of the Royal Society of London Series a-Mathematical and Physical Sciences* **164**, 0192 (1938).
- [44] G. K. Batchelor, *The Theory of Homogeneous Turbulence* (Cambridge University Press, Cambridge, UK, 1953).
- [45] A. N. Kolmogorov, *Journal of Fluid Mechanics* **13**, 82 (1962).
- [46] J. M. Colberg, S. D. M. White, A. Jenkins, and F. R. Pearce, *Monthly Notices of the Royal Astronomical Society* **308**, 593 (1999).
- [47] R. K. Sheth, H. J. Mo, and G. Tormen, *Monthly Notices of the Royal Astronomical Society* **323**, 1 (2001).
- [48] P. J. E. Peebles, *The Large-Scale Structure of the Universe* (Princeton University Press, Princeton, NJ, 1980).
- [49] Z. Xu, *arXiv e-prints*, [arXiv:2110.05784](https://arxiv.org/abs/2110.05784) (2021).
- [50] Z. Xu, *arXiv e-prints*, [arXiv:2109.09985](https://arxiv.org/abs/2109.09985) (2021).
- [51] Z. Xu, *Scientific Reports* **13**, 4165 (2023), [arXiv:2209.03313](https://arxiv.org/abs/2209.03313) [astro-ph].
- [52] R. K. Sheth, *Monthly Notices of the Royal Astronomical Society* **279**, 1310 (1996).
- [53] E. Romano-Díaz and R. Van De Weygaert, *Monthly*

- Notices of the Royal Astronomical Society **382**, 2 (2007), <https://academic.oup.com/mnras/article-pdf/382/1/2/3056346/mnras0382-0002.pdf> .
- [54] F. Bernardeau and R. vandeWeygaert, *Monthly Notices of the Royal Astronomical Society* **279**, 693 (1996).
- [55] W. M. Irvine, *Local Irregularities in a Universe Satisfying the Cosmological Principle*, Thesis, HARVARD UNIVERSITY (1961).
- [56] D. Layzer, *Astrophysical Journal* **138**, 174 (1963).
- [57] H. J. Mo, Y. P. Jing, and G. Borner, *Monthly Notices of the Royal Astronomical Society* **286**, 979 (1997).
- [58] Z. Xu, *arXiv e-prints* , arXiv:2202.04054 (2022).
- [59] R. K. Sheth, L. Hui, A. Diaferio, and R. Scoccamarro, *Monthly Notices of the Royal Astronomical Society* **325**, 1288 (2001), <https://academic.oup.com/mnras/article-pdf/325/4/1288/3030319/325-4-1288.pdf> .
- [60] Z. Xu, “Dark matter flow dataset part i: Halo-based statistics from cosmological n-body simulation,” (2022).
- [61] Z. Xu, “Dark matter flow dataset part ii: Correlation-based statistics from cosmological n-body simulation,” (2022).
- [62] Z. Xu, “A comparative study of dark matter flow & hydrodynamic turbulence and its applications,” (2022).
- [63] Z. Xu, “Dark matter flow dataset,” (2022).